Pergamon

Journal of Structural Geology, Vol. 16, No. 4, pp. 531 to 553, 1994

0191-8141/94 $06.00 + 0.00

0191-8141(93)E0008-9

Non-volatile element and volume flux in coalesced slaty cleavage

ERIC A. ERSLEV and DAVID J. WARD*

Department of Earth Resources, Colorado State University, Fort Collins, CO 80523, U.S.A.

(*Received* 16 *January* 1993; *accepted in revised form* 1 *November* 1993)

Abstract—Non-volatile element and volume flux during slaty cleavage formation was determined by mapping major element compositions in hand specimens of slate with variable cleavage intensity due to non-argillaceous interlayers. Intense spaced cleavage zones form where cleavage coalesces within the inner arcs of folded non-argillaceous layers or at the offsets between imbricated non-argillaceous layers.

The element distributions in samples from Nova Scotia, Vermont and New Jersey were mapped using an XRF-macroprobe, an energy dispersive XRF with automated spectrum acquisition and a mm-scale collimated beam. Cleavage zones are depleted in quartz and SiO_2 and enriched in phyllosilicates, Al_2O_3, Fe_2O_3, K_2O, MgO and TiO_2. CaO and MnO show more variable behavior consistent with simultaneous depletion in carbonates and residual enrichment in silicates. Quartz-rich, weakly cleaved areas adjacent to fold outer arcs or between imbricate offsets are enriched in quartz with respect to probable pre-cleavage compositions, with SiO_2 commonly reaching 75–80 wt%. The spaced cleavage zones and their intervening microlithons grade texturally and compositionally into penetrative cleavage with distance from non-argillaceous layering.

Average compositions of heterogeneously cleaved beds are quite similar to compositions of homogeneously cleaved beds in the same sample, suggesting balanced, localized element enrichment and depletion adjacent to non-argillaceous layers. The similarities between average macroprobe, slate and shale compositions suggest minimal non-volatile net volume flux during the formation of slaty cleavage. Volume losses of 50% by SiO_2 flux would result in a rock with approximately equal SiO_2 and Al_2O_3 wt%, not a slate. Most of the non-volatile element and volume flux in the slates occurred on a hand specimen scale, with quartz depletion in cleavage zones balanced by enrichment in adjoining microlithons.

INTRODUCTION

GEOMETRICAL and geochemical determinations of volume flux during slaty cleavage formation are often contradictory. Numerous studies have used geometric fabric information to argue for substantial (e.g. 25–60%) volume loss of non-volatile components during slaty cleavage development (Sorby 1853, Wright & Platt 1982, Bell 1985, Beutner & Charles 1985, Henderson *et al.* 1988, Wright & Henderson 1992). Geochemical studies of cleavage zones (P domains) and uncleaved microlithons (Q domains) show considerable compositional contrasts consistent with material flux out of spaced cleavage zones (Stephens *et al.* 1979, Erslev & Mann 1984, Clifford *et al.* 1987, Lincoln 1988, Sutton 1989). But similarities between whole-rock analyses of slates and shales suggest very little net flux of non-volatile elements (excluding volatile pore fluids) during the formation of slates (Shaw 1956, Wintsch *et al.* 1991, Ague 1991).

This paper tests the hypothesis of substantial non-volatile element and volume flux during slaty cleavage formation by documenting mm- to dm-scale compositional changes in slates with heterogeneously cleaved beds. Hand specimens of slate with bed-parallel variations in cleavage intensity were acquired from the Meguma Group of Nova Scotia, the Mettawee Formation of southwest Vermont, and the Martinsburg Formation of western New Jersey. In all of the samples, penetrative slaty cleavage coalesces to form cm-scale spaced cleavage adjacent to shortened veins or arenite layers.

Geochemical data were collected using an XRF-macroprobe which was designed and constructed specifically for the mm-scale spatial resolution needed for this project (Fig. 1). The macroprobe is an energy dispersive X-ray system with a collimated X-ray beam, an automated *x–y* stage and computer-facilitated spectrum acquisition.

This paper has two main objectives. First, the compositional differences between cleaved and uncleaved parts of the same bed will be used to document the mobility of

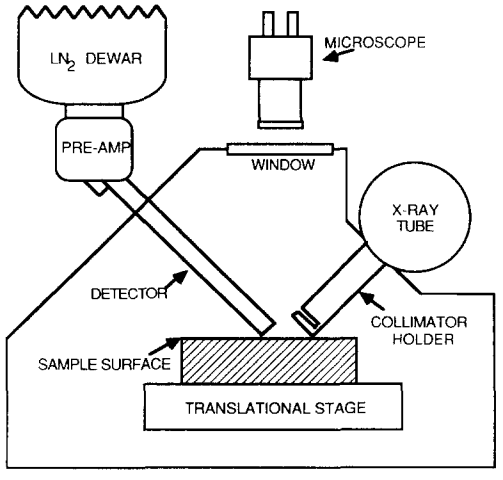

Fig. 1. Schematic diagram of the XRF-macroprobe.

*Current address: Dames and Moore, 1701 Golf Road, Suite 1000, Rolling Meadows, IL 60008, U.S.A.

individual elements during the development of slaty cleavage. Second, macroprobe and average pelite compositions will be used to limit the scale and magnitude of non-volatile volume flux in slates.

PREVIOUS WORK

The possibility of extensive volume flux in slates has been proposed by structural studies of slate fabrics. Sorby (1853) showed that a volume loss of 60% could account for the strained reduction spots in Welsh slates without necessitating elongation of the strain axes in the plane of the cleavage. Ramsay & Wood (1973) plotted the dimensions of strained reduction spots from 990 slates on a Flinn diagram and found that they fell within the flattening field. They suggested that this could be the result of true distortional flattening or plane strain accompanied by volume loss. Bell (1985) determined that a combination of diagenetic compaction, cleavage-normal volume loss and plane strain distortion was needed to replicate strained accretionary lapilli in metavolcanics of the English Lake District.

Wright & Platt (1982) showed that where bedding in the Martinsburg slate from central Pennsylvania was perpendicular to cleavage, graptolites were shortened normal to cleavage. The lack of equivalent extension in other localities where beds parallel cleavage was used to propose up to 50% volume loss normal to cleavage. Beutner & Charles (1985) studied cleavage formation in nearby Hamburg sequence slates by comparing extension in conodonts to deformed reduction spots. They also concluded that shortening perpendicular to cleavage was not compensated by cleavage-parallel extension, necessitating 29–42% volume loss. In contrast, Groshong (1976) found quartz overgrowths on quartz grains between cleavage laminae in the Martinsburg slate from New Jersey and hypothesized that pressure solution mobilization and local redistribution of silica occurred without substantial volume loss. Working in the same locality, Beutner *et al.* (1977) determined that cleavage-perpendicular shortening was compensated by cleavage-parallel stretching.

Henderson *et al.* (1988) compared shortening strain calculated from buckled, bedding-parallel quartz veins to strain indicated by the aspect ratios of deformed sand volcanoes in the Goldenville Formation of the Meguma Group in Nova Scotia. They found little evidence for extension in the cleavage plane despite considerable cleavage-perpendicular shortening, suggesting that 40–60% of the rock volume was removed during cleavage formation (Henderson *et al.* 1988). Wright & Henderson (1992) showed that worm burrow geometries in the Meguma slates suggest minimal vertical stretching of the units, indicating 60% volume loss.

Geochemical studies, however, argue against substantial volume loss in slates. In fact, isochemical (with the exception of volatiles) metamorphism of pelites is a common assumption in studies of crustal evolution which use pelitic compositions to monitor crustal changes through time (Condie 1981, Taylor & McLennan 1985, Gibbs *et al.* 1986). Average shale and slate compositions show very little difference in their compositions. Table 1 lists previously published average pelite compositions with and without volatiles (H_2O and CO_2), allowing the comparison of pelites at different stages of metamorphic devolatilization. Shaw (1956) compared 155 analyses of pelitic rocks from shales to high-grade metamorphic rocks and found no statistically significant changes in composition during regional metamorphism. Ague (1991) re-examined this and subsequent data and found evidence for up to 30% non-volatile volume loss during metamorphism. But he attributed this volume loss to medium and high grades of metamorphism and lumped shales and slates together to represent initial compositions.

Kanagawa (1991) compared the chlorite fabric intensity of slates from the Kitkami Mountains of northeast Japan with their bulk chemistry. He found no systematic compositional changes with changes in fabric intensity, concluding that slaty cleavage development did not affect bulk composition on a hand specimen scale. Wintsch *et al.* (1991) analyzed changes in bulk composition and specific gravity across a transition from shale to slate in Martinsburg Formation railroad cuts at Lehigh Gap, Pennsylvania. They found evidence for km-scale depletion of minor components such as CaO, Na_2O and Ba in slates, but these elements make up a very small proportion of the bulk rock volume. The other major elements in the pelites do not change significantly through the transition, indicating that fabric changes at this locality were not accompanied by significant volume changes (Wintsch *et al.* 1991).

The profound discrepancy between structural determinations of volume loss and geochemical evidence for a lack of volume loss during slaty cleavage development is the rationale for this study. Either volume loss related to cleavage formation is extremely heterogeneous, involving large volume losses in some cases and volume-constant, localized element redistribution in others, or data from some localities have been misinterpreted.

XRF-MACROPROBE METHODS

One problem plaguing previous studies of element variability in cleaved rocks is the fact that conventional whole-rock XRF and electron microprobe techniques were not designed to document changes in rock composition at the mm to cm scale. The analyses used in this study were collected using an XRF-macroprobe (Fig. 1), an instrument designed and assembled at Colorado State University for this research project by N. L. Gilfrich Tucker and D. E. Leyden of the Department of Chemistry. The instrument was designed to collect semi-quantitative whole-rock compositions at the millimeter to centimeter scale without destroying the sample. Instrument specifications and error analysis from Gilfrich *et al.* (1990) are presented in the Appendix.

X-ray excitation of the sample has the following

JSG 16:4-G

Table 1. Average shale and slate compositions

	Average shales									
	Clarke (1924)		Gromet *et al.* (1984, microprobe)		Gromet *et al.* (1984, XRF)		Krauskopf (1967)		Taylor & McLennan (1990)	
n:	78		40 (NASC)		40 (NASC)		(not given)		(not given)	
	Average	Normalized	Average	Normalized	Average	Normalized	Average	Normalized	Average	Normalized
SiO_2	58.11	63.76		64.49		64.28	50.19	61.07	62.8	63.70
TiO_2	0.65	0.71		0.78		0.79	0.75	0.99	1.0	1.01
Al_2O_3	15.40	16.91		16.81		16.91	15.12	18.14	18.9	19.17
Fe_2O_3	6.74	7.40		6.24		6.28	6.72	8.15	7.2	7.32
MnO				0.06		0.25		0.11	0.11	0.11
MgO	2.44	2.68		2.84		2.81	2.22	2.68	2.2	2.23
CaO	3.10	3.41		3.60		3.48	3.50	4.16	1.3	1.32
Na_2O	1.30	1.43		1.13		1.12	0.89	1.09	1.2	1.22
K_2O	3.24	3.55		3.91		3.94	2.77	3.37	3.7	3.75
P_2O_5	0.17	0.13		0.14		0.15	0.18	0.22	0.16	0.16
S							0.02	0.02		
Volatiles	7.62								6.0	
Total	98.77	100.00		100.00		100.00	83.37	100.00	104.57	100.00

	Mixed shales and slates				**Slates**					
Source:	Ague (1991)		Wintsch *et al.* (1991)		Eckel (1904)		Bastin (1909)		CSU-1 (Standard)	
n:	105		50		36		79		1	
	Average	Normalized	Average	Normalized	Average	Normalized	Average	Normalized	Analysis	Normalized
SiO_2	60.34	63.46	62.23	65.37	60.64	64.59	60.49	63.66	57.0	61.15
TiO_2	0.76	0.80	1.08	1.14	0.73	0.78	0.73	0.77	0.79	0.85
Al_2O_3	17.05	17.93	16.71	17.55	17.32	18.45	17.56	18.48	15.3	16.41
Fe_2O_3	7.37	7.75	7.57	7.95	6.32	6.73	7.86	8.26	8.33	8.94
MnO	0.09	0.09	0.04	0.04					0.07	0.08
MgO	2.69	2.83	2.72	2.86	2.60	2.77	2.51	2.64	3.18	3.41
CaO	1.45	1.53	0.12	0.13	5.23	1.64	1.26	1.32	3.68	3.95
Na_2O	1.55	1.63	0.37	0.39	1.19	1.27	1.32	1.39	1.28	1.37
K_2O	3.64	3.83	4.05	4.26	3.69	3.78	3.31	3.48	3.42	3.67
P_2O_5	0.14	0.15	0.29	0.31					0.16	0.17
S									0.72	0.77
Volatiles	4.80		5.13		4.98		5.03		5.30	
Total	99.88	100.00	100.32	100.00	102.70	100.00	100.07	100.00	99.23	100.00

Table 2. Summary of macroprobe analyses

Unit:	Martinsburg Slate, New Jersey						Mettawee Slate, Vermont			
Sample:	CM3A		M1A		DG2-2		VT1T		VT1M	
n:	66		38		1709		78		275	
Spot area (mm^2):	19		19		19		19		19	
	Average	Normalized	Average	Normalized	Average	Normalized	Average	Normalized	Average	Normalized
SiO_2	57.93	64.30	59.96	66.17	57.19	57.56	55.55	63.66	55.58	61.95
TiO_2	0.73	0.81	0.73	0.81	0.67	0.67	0.71	0.81	0.79	0.88
Al_2O_3	14.78	16.41	14.91	16.45	18.68	18.80	15.47	17.73	16.79	18.72
Fe_2O_3	7.53	8.36	7.09	7.82	8.66	8.72	7.16	8.21	7.91	8.82
MnO	0.061	0.068	0.032	0.035	0.096	0.097	0.140	0.160	0.107	0.119
MgO	2.46	2.73	1.88	2.07	4.49	4.52	2.79	3.20	2.83	3.15
CaO	1.69	1.88	0.75	0.82	3.16	3.18	1.24	1.42	1.02	1.14
K_2O	3.90	4.33	4.25	4.69	4.78	4.81	4.20	4.81	4.68	5.22
S	1.01	1.12	0.99	1.09	1.62	1.63				
Difference	9.91		9.40		0.65		12.74		10.29	
Total	100.00	100.00	99.99	99.97	100.00	99.99	100.00	100.00	100.00	99.99

Regression vs Al_2O_3

	y-intercept	*x* coefficient	R^2	*y*-intercept	*x* coefficient	R^2	*y*-intercept	*x* coefficient	R^2	*y*-intercept	*x* coefficient	R^2	*y*-intercept	*x* coefficient	R^2
SiO_2	84.4	−1.79	0.81	91.09	−2.09	0.74	88.79	−1.69	0.86	71.12	−1.01	0.35	80.34	−1.48	0.71
TiO_2	−0.22	0.065	0.82	−0.47	0.08	0.96	−0.37	0.056	0.55	−0.11	0.05	0.80	−0.15	0.056	0.83
Fe_2O_3	1.73	0.393	0.82	0.30	0.46	0.58	1.53	0.38	0.78	0.30	0.44	0.90	3.12	0.29	0.67
MnO	0.16	−0.007	0.50	0.083	−0.003	0.19	0.16	−0.003	0.16	0.34	−0.013	0.13	0.24	−0.008	0.18
MgO	1.13	0.09	0.24	0.44	0.096	0.38	1.67	0.15	0.33	−0.021	0.18	0.08	0.12	0.16	0.14
CaO	4.57	−0.19	0.25	2.72	−0.13	0.47	5.99	−0.15	0.16	2.72	−0.095	0.30	1.91	−0.053	0.11
K_2O	−0.37	0.29	0.93	−0.59	0.32	0.99	−0.55	0.29	0.97	−0.96	0.33	0.96	−1.37	0.36	0.97
S	−0.29	0.088	0.32	1.12	−0.009	0.01	−0.66	0.12	0.32						

Unit:	Meguma Slate, Nova Scotia									
Sample:	MEG1A		MEG1B		MEG1C		MEG2A+B		MEG2C+D	
n:	80		557		43		78		1015	
Spot area (mm^2):	110		19		19		19		19	
	Average	Normalized	Average	Normalized	Average	Normalized	Average	Normalized	Average	Normalized
SiO_2	68.58	68.65	62.50	63.41	66.83	69.53	63.96	64.02	61.15	61.91
TiO_2	0.65	0.65	0.72	0.73	0.55	0.57	0.75	0.75	0.80	0.81
Al_2O_3	19.07	19.09	22.07	22.39	17.73	18.45	22.26	22.28	23.38	23.67
Fe_2O_3	6.30	6.31	7.21	7.32	6.41	6.67	6.76	6.77	6.98	7.07
MnO	0.034	0.034	0.038	0.039	0.029	0.030	0.036	0.036	0.040	0.040
MgO										
CaO	0.31	0.31	0.44	0.45	0.27	0.28	0.26	0.26	0.29	0.29
K_2O	4.85	4.86	5.47	5.55	4.21	4.38	5.73	5.73	6.03	6.11
S	0.09	0.09	0.09	0.09	0.07	0.07	0.13	0.13	0.12	0.12
Difference	0.11		1.45		3.89		0.10		1.22	
Total	99.99	99.99	99.99	99.98	99.99	99.98	99.99	99.97	100.01	100.02

Regression vs Al_2O_3

	y-intercept	*x* coefficient	R^2	*y*-intercept	*x* coefficient	R^2	*y*-intercept	*x* coefficient	R^2	*y*-intercept	*x* coefficient	R^2	*y*-intercept	*x* coefficient	R^2
SiO_2	98.3	−1.56	0.99	93.8	−1.42	0.97	91.86	−1.41	0.89	97.83	−1.52	0.99	94.87	−1.44	0.93
TiO_2	0.010	0.034	0.21	−0.16	0.040	0.11	−0.30	0.048	0.03	0.007	0.033	0.10	0.027	0.033	0.07
Fe_2O_3	1.52	0.25	0.90	1.79	0.25	0.86	2.29	0.23	0.75	1.60	0.23	0.93	2.31	0.20	0.79
MnO	0.002	0.002	0.59	0.004	0.001	0.20	−0.006	0.002	0.25	−0.001	0.002	0.66	0.016	0.001	0.15
MgO															
CaO	0.20	0.006	0.10	0.27	0.008	0.01	0.042	0.013	0.14	0.064	0.009	0.50	0.18	0.005	0.03
K_2O	−0.15	0.26	0.99	−0.22	0.26	0.99	0.033	0.24	0.99	−0.13	0.26	0.997	−0.33	0.27	0.98
S	0.071	0.001	0.03	0.068	0.001	0.02	0.032	0.002	0.11	0.086	0.002	0.06	0.12	−0.000	0.00

advantages over electron beam excitation used by electron probe and SEM instruments.

(1) X-ray beams do not require a conductive surface coating or the degree of polish required by electron beam methods.

(2) X-ray beams are not focused and thus do not require as exact source-to-sample distances. This allows automated element mapping of large surfaces without constant adjustment of sample elevation.

(3) The stability of X-ray tubes and energy dispersive detectors, relative to electron beams, allows long duration analyses.

(4) The greater effective X-ray excitation depth results in 10 times more material sampled than the analysis of an equivalent area by electron beam methods (Boehme 1987).

(5) Relative to electron beam methods, X-ray excitation of samples results in less background radiation and clearer definition of the peaks of characteristic X-rays.

Macroprobe data presentation

The average macroprobe analyses for each map and traverse are presented in Table 2. These values are reported with non-significant figures because the accuracy of the analyses differs for each sample (see the Appendix for a detailed discussion). Data sets for individual samples were culled to eliminate analyses with anomalously high differences (often due to voids or epoxy), $Al_2O_3 < 9.0$ wt% and high CaO. The remaining analyses are presented in plots of oxides and S vs Al_2O_3 to show compositional variability within samples and to highlight element mobilities relative to a common reference frame. Ideally, a plot of a potentially mobile component on the y-axis vs a truly immobile component on the x-axis can be used to determine the behavior of the potentially mobile component (Fig. 2). If the components are equally immobile, they will plot in an array with a positive slope and a y-intercept of 0.0 due to either accumulation as a residue during volume loss or dilution during volume gain. Component mobility due to enrichment by addition to the system or depletion by flux from the system will be shown as data arrayed about a line with a negative slope.

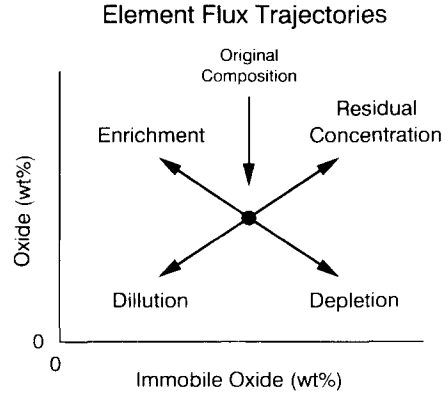

Fig. 2. Idealized behavior of components plotted vs an insoluble oxide.

The two obvious candidates for an immobile component are Al_2O_3 and TiO_2. Studies of element solubility in low-CO_2 fluids suggest that Al_2O_3 and TiO_2 are usually the least soluble major element oxides (O'Hara & Blackburn 1989, Ghent & Gordon 1990, Ague 1991). These two oxides are plotted against each other in Fig. 3 for representative macroprobe analyses. Samples M1A, CM3A and VT1M show linear relationships between the oxides consistent with immobile behavior for both oxides. In DG2-2, TiO_2 increases dramatically at higher Al_2O_3 contents, suggesting Al_2O_3 mobility at high TiO_2 content. The large scatter in TiO_2 for sample MEG2C+D is due to TiO_2 redistribution in sphene porphyroblasts. Al_2O_3 was chosen as a reference frame for these plots due to its greater concentration and the localized Ti redistribution in the important Meguma samples (Wright & Henderson 1992) despite the apparent mobility of Al relative to Ti in Martinsburg sample DG2-2. Regression line intercepts and R^2 values of oxides and S relative to Al_2O_3 are given in Table 2 for each set of analyses.

MEGUMA SLATE, NOVA SCOTIA

Slate samples MEG1 and MEG2 are from the Cambrian–Early Ordovician Goldenville Formation of the Meguma group in the Moose River gold district of Nova Scotia, Canada. These samples consist of fresh drill cores of dark gray slate cut by bedding-parallel, buckled veins approximately 5 mm in thickness (Figs. 4a & b). The vein in MEG1 is composed of calcite with minor quartz, whereas quartz dominates the vein in MEG2, which was featured on the cover of *Geology* in July 1990. Concentrations of arsenopyrite are common in both veins where they thin. Minimum shortening perpendicular to cleavage, measured by unfolding the veins, is 59% for MEG1 and 65% for MEG2. The penetrative, axial planar cleavage does not cut the veins and is most intense within the inner arcs of the folds.

Slate within fold inner arcs is composed almost entirely of aligned muscovite grains, giving the inner arc parallel extinction and higher birefringence than surrounding areas. Material adjacent to outer arcs is quartz rich, with muscovite orientations approaching randomness near the outer arcs of folds. Cleavage becomes more evenly penetrative with distance from the veins. Pyrite grains and aggregates of porphyroblastic sphene are concentrated in inner arc areas. Many pyrite grains and sphene aggregates have pressure shadows of quartz and muscovite oriented parallel to cleavage. Sphene aggregates are equant in outer arcs and elongate parallel to cleavage in inner arcs. Where these aggregates have pulled apart parallel to cleavage, quartz fills the intervening areas. Chlorite grains are abundant and commonly oriented with basal planes perpendicular to cleavage.

Chemical data were collected from the samples in

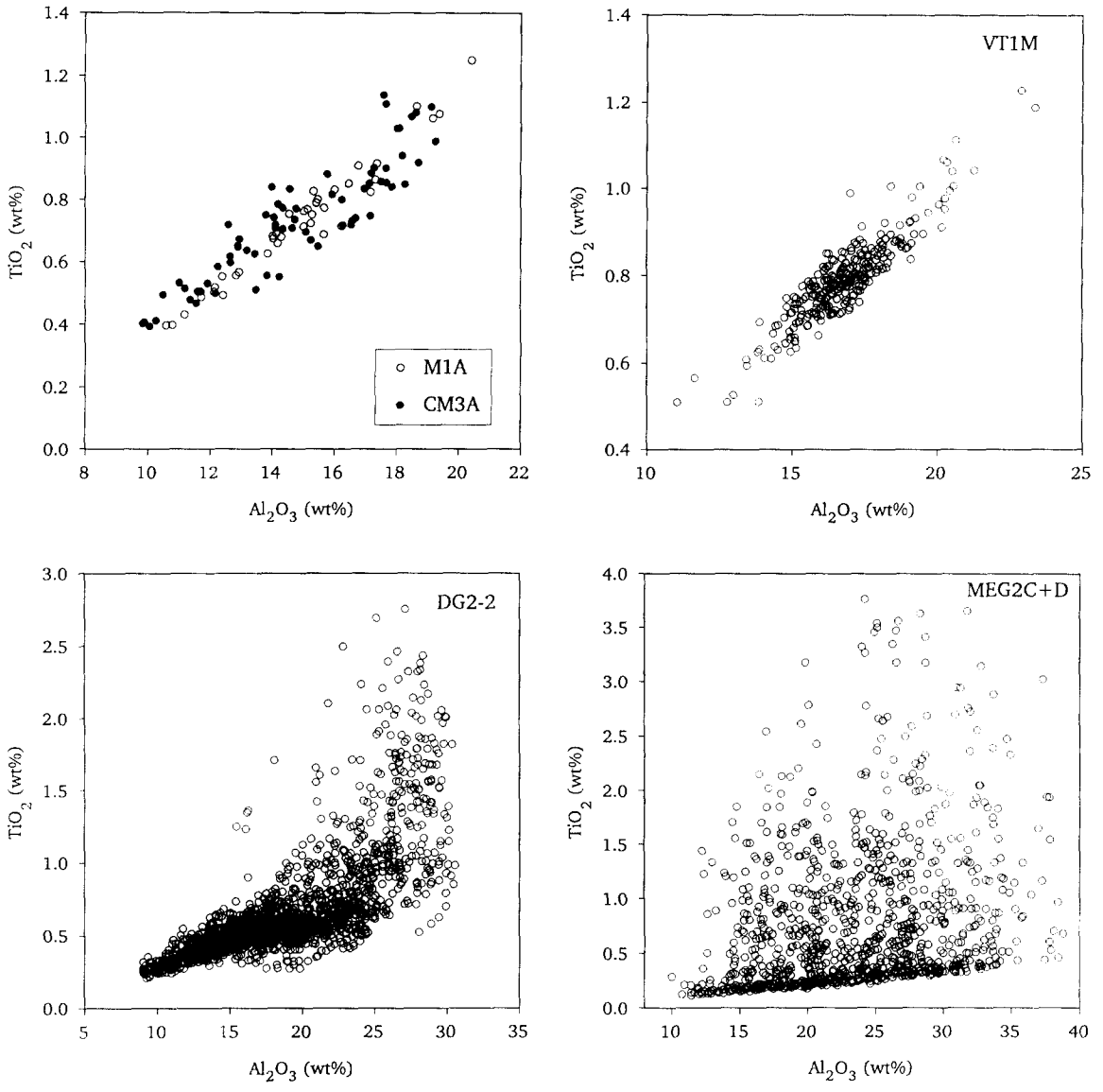

Fig. 3. TiO_2 plotted vs Al_2O_3 for the samples analyzed in this study.

Figs. 4(a) & (b), including three individual traverse analyses (MEG1C, MEG2A and MEG2D) and three map analyses (MEG1B, MEG2C and MEG2D). Oxide concentrations are plotted vs distance along bedding-parallel traverse MEG2A in Fig. 5. The areas with intense cleavage show enrichment in Al, Fe, K and Ti with depletion of Si relative to the less cleaved outer arcs of the folds. The highest silica values, ranging to 78 wt% SiO_2, come from slate immediately adjacent to fold outer arcs. Fold inner arc areas, where cleavage is most intense, are enriched in Al, Fe, K and Mn, with SiO_2 as low as 47 wt%.

Contour maps of SiO_2, Al_2O_3, K_2O, Fe_2O_3 and TiO_2 were compiled from map analysis MEG1B (Fig. 6). SiO_2 is highest (up to 79 wt%) in triangle-shaped zones adjacent to fold outer arcs and lowest (down to 39 wt%) in the intensely cleaved fold inner arcs. Both areas of high and low SiO_2 taper and terminate away from the veins. Al_2O_3, K_2O and Fe_2O_3 show the opposite pattern, with high values in the inner arcs and low values in the outer arcs. TiO_2 shows a spotty distribution due to concentration in sphene porphyroblasts.

Oxide and sulfur compositions from map analyses MEG1B and MEG2C+D were plotted vs Al_2O_3 in Figs. 7 and 8. All individual analyses with more than 2.0 wt% CaO or less than 9.0 wt% Al_2O_3 were interpreted to include vein material and were excluded from the plots. Fe_2O_3 and K_2O show strong positive linear correlations with Al_2O_3. MnO and CaO are positively correlated to Al_2O_3, but the relationships show some scatter. Considering the lack of carbonate minerals in the slate and the positive correlation between MnO and CaO with Al_2O_3, these elements are probably in silicates and sphene. Plots of TiO_2 vs Al_2O_3 have widely scattered data above linear baselines which may represent TiO_2 in phyllosilicates. Scatter above baselines is due to local Ti concentration in metamorphic sphene aggregates. S shows little correlation with Al_2O_3 because it is not abundant in the rock, with high data points indicating isolated sulfide grains.

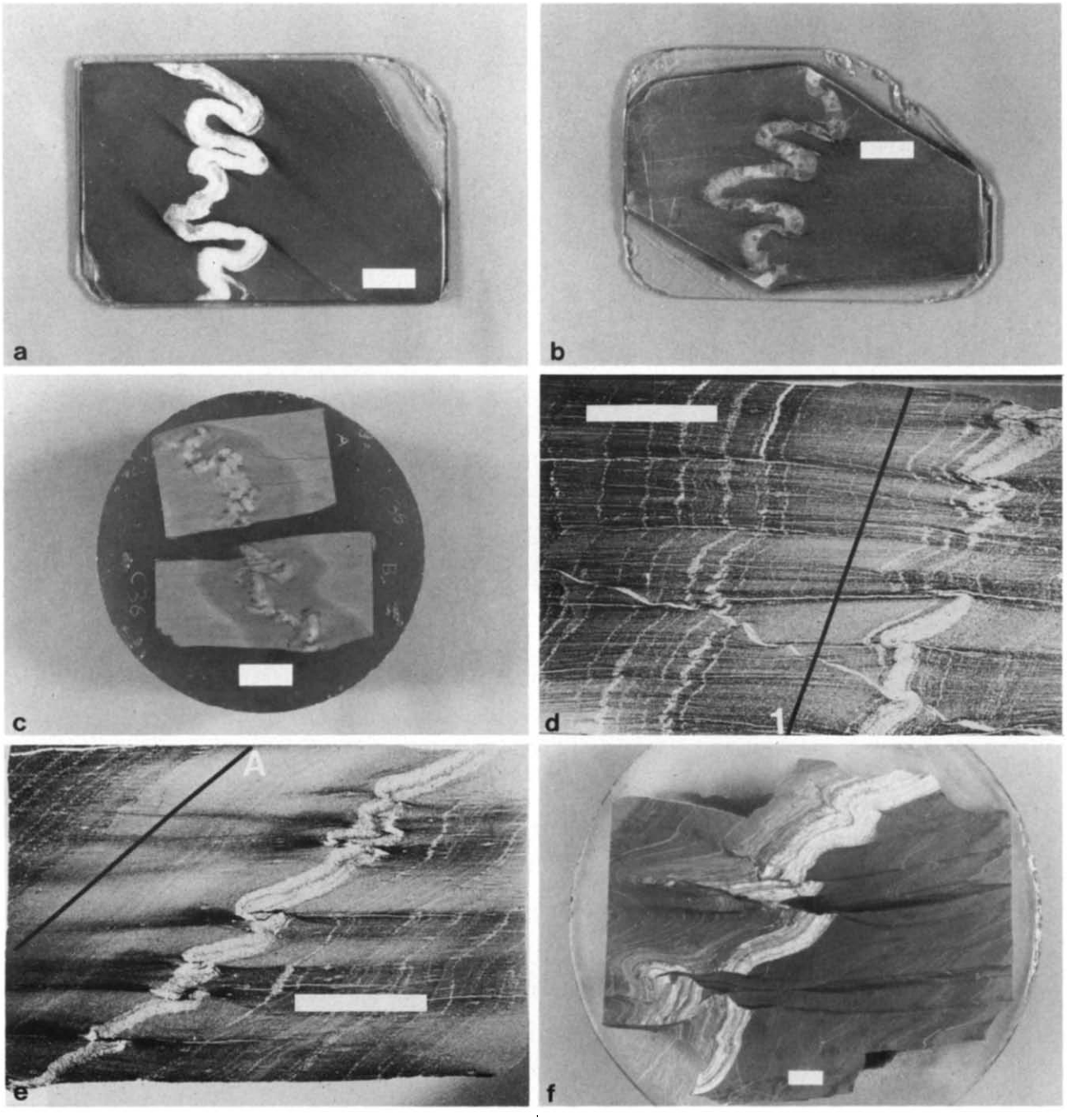

Fig. 4. Thin section and hand specimen photographs of samples analyzed in this study: Meguma Group slates (a) MEG1 and (b) MEG2; (c) Mettawee Formation slate; and Martinsburg Formation slates (d) CM3A, (e) M1A, and (f) DG2-2. White scale bars are 1 cm in length.

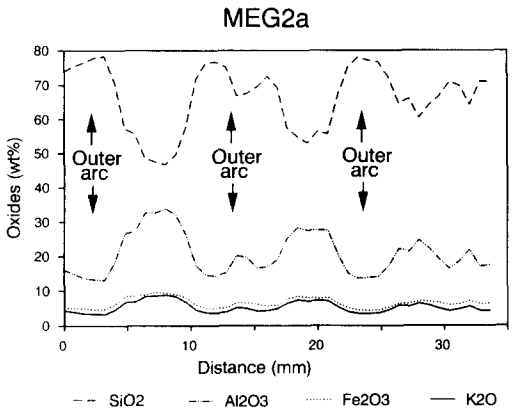

Fig. 5. Composition vs distance for analysis MEG2A.

METTAWEE SLATE, VERMONT

Sample VT1 (Fig. 4d) was collected from an abandoned slate quarry in the Cambrian Mettawee Formation of the Taconic sequence southeast of Fairhaven, Vermont. Reduction spot dimensions from this quarry suggest 70% shortening perpendicular to cleavage (A. Goldstein 1992 personal communication). Complex pressure shadows on euhedral pyrite crystals give minimal cleavage-parallel extensions, suggesting large volume losses. The sample consists of a poorly bedded green slate cut by a ptygmatically folded quartz–calcite vein. Buckle folding of the vein gives a minimum cleavage-perpendicular shortening of 50%.

Macroprobe analysis VT1T consists of two closely spaced, vein-parallel traverses crossing two thin section chips embedded in epoxy (Fig. 9). In general, SiO_2 decreases in areas of more intense cleavage within the inner arcs of folds and increases adjacent to the outer arc of folds. Al_2O_3, Fe_2O_3 and K_2O show opposite behavior, increasing in more highly cleaved areas and decreasing in less cleaved areas. The second chip was mapped in analysis VT1M to show the detailed element distribution (Fig. 10). The SiO_2 and Al_2O_3 values in Fig. 10 show that both the most and least siliceous zones are immediately adjacent to the vein. The inner arc of the folds contain both the most highly cleaved and the least siliceous slate. The outer arcs of the folds are the most siliceous. The differences in the slate compositions decrease with distance from the vein.

Analyses VT1T and VT1M plotted vs Al_2O_3 (Fig. 11) show a positive correlation between Al_2O_3 and Fe_2O_3, K_2O and TiO_2 without the complications due to sphene crystallization in the Meguma samples. SiO_2 is negatively correlated with Al_2O_3. CaO and MnO are scattered, with a general negative correlation with Al_2O_3 suggesting element mobility relative to Al. MgO shows a positive correlation in both cases but with considerable scatter.

MARTINSBURG SLATE

Three samples were collected from an outcrop of the Bushkill member of the Ordovician Martinsburg Formation located 3 km northeast of Belvidere, New Jersey, along U.S. Route 54 (Ward 1991). At this outcrop, grey slate is interlayered with thin beds of dolomite siltstone. Slaty cleavage is at a high angle to the homogeneous slate beds and is axial planar to asymmetrical folds in thick (20–30 cm) dolomite beds. Within 2 m of the beds, cleavage fans around the outer arcs of the folds, becoming tangent to the fold limbs. Smaller dolomite laminae are imbricated and cut by coalesced cleavage at offsets between imbricate segments. Minimum cleavage-perpendicular shortening calculated from the folded beds is 43% (Erslev & Mann 1984). Pressure shadows on pyrite framboids give cleavage-parallel extensions ranging from 90 to 160% (Ward 1991) using the method of Durney & Ramsay (1973).

CM3A and M1A

Samples CM3A (Fig. 4d) and M1A (Fig. 4e) consist of silty slate with dolomite laminae. The thickest dolomite layer in each sample is imbricated, with slaty cleavage coalescing at layer offsets and strain shadows developing between offsets. Minimum shortening of bedding calculated from the imbricated dolomite layers is 37% for CM3A and 23% for M1A. CM3A is also cut by an oblique carbonate vein (from middle left to lower right in Fig. 4d) whose offsets along the zones of coalesced cleavage have the same shear sense as the offsets of the bed. This geometry is inconsistent with dissolution as the only cause of the offsets.

Most quartz grains are elliptical, with long axes parallel to cleavage-parallel phyllosilicates, except in small lensoidal domains of undeformed slate adjacent to more competent layers (Erslev & Mann 1984). Quartz grain ellipticity increases with an apparent decrease in modal abundance within zones of coalesced cleavage (Ward 1991).

Macroprobe traverses for each sample were oriented parallel to bedding and within the most homogeneous layer with coalesced cleavage zones. The traverses (Fig. 12) show clear SiO_2 depletion and simultaneous Al_2O_3, Fe_2O_3 and K_2O enrichment in the areas of intense cleavage with respect to less cleaved microlithons. When plotted vs Al_2O_3 (Fig. 13), Fe_2O_3, K_2O and TiO_2 show excellent linear relationships with positive slopes and near zero y-axis intercepts consistent with immobile behavior. SiO_2 concentrations, in contrast, define an array with a negative slope indicating mobile behavior. CaO and MnO show less well defined negative slopes which also suggest mobility relative to Al_2O_3. MgO and S values show great scatter but generally indicate enrichment with Al_2O_3.

DG2-2

Sample DG2-2 (Fig. 4f) was removed from the outcrop using a coring drill and consists of dark gray slate interlayered with silty dolomite laminae. A 15–20 mm thick, bed-parallel crack–seal calcite vein is folded and

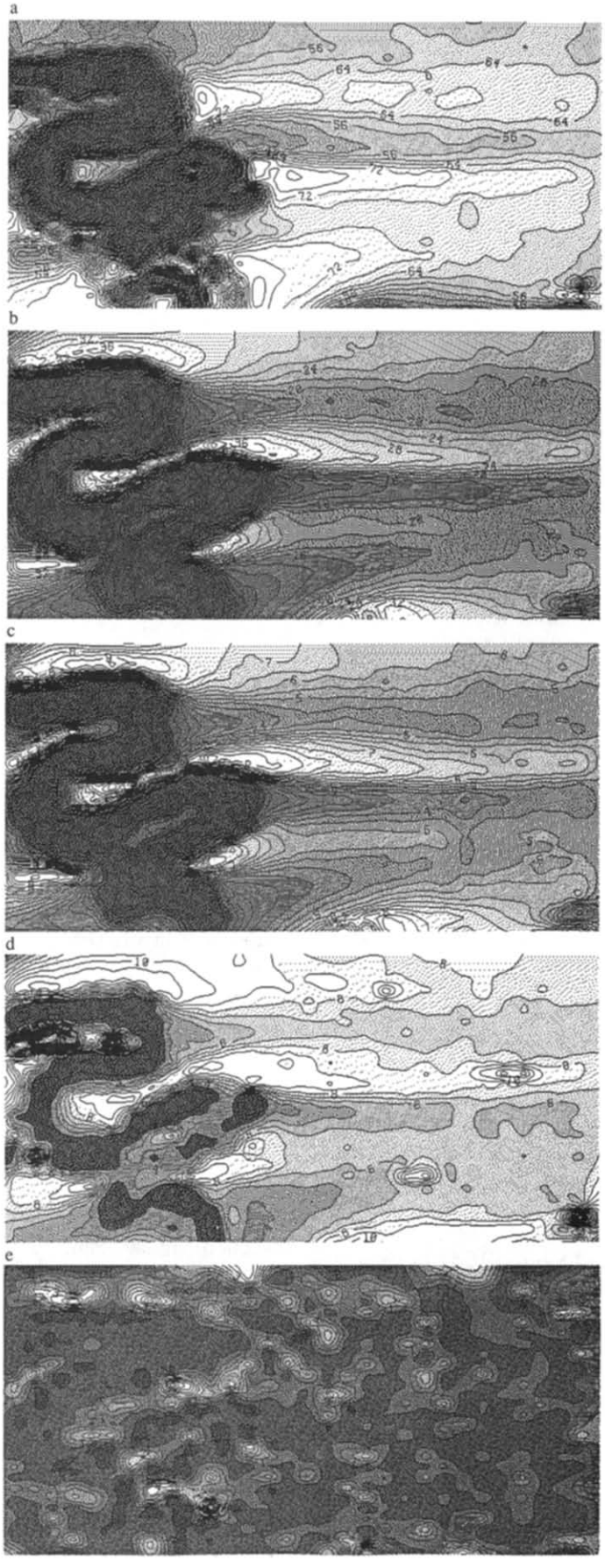

Fig. 6. Contoured (a) SiO_2, (b) Al_2O_3, (c) K_2O, (d) Fe_2O_3 and (e) TiO_2 element maps from analysis MEG1B. Light areas indicate high values.

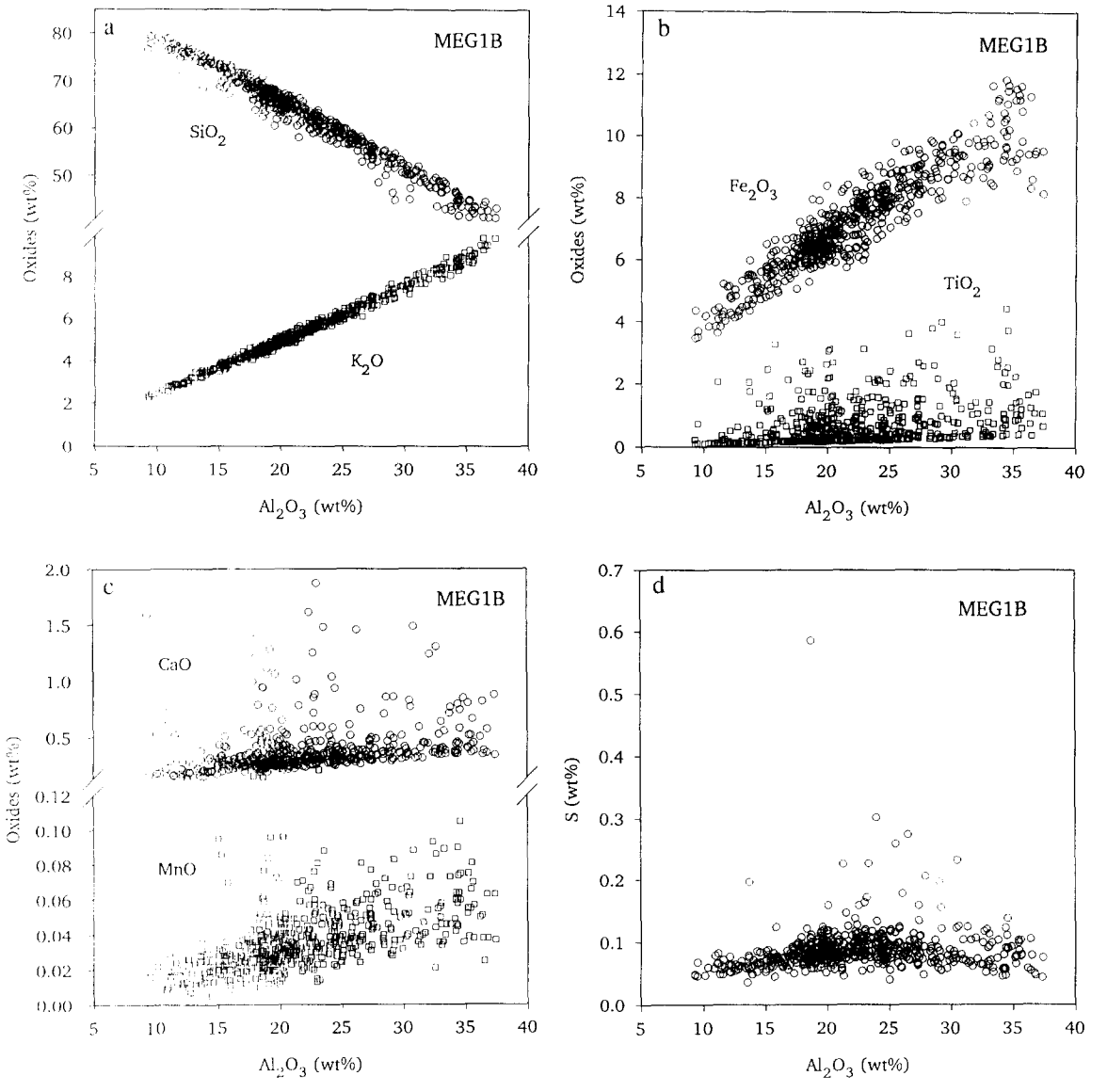

Fig. 7. Variation diagrams showing: (a) SiO_2 and K_2O; (b) Fe_2O_3 and TiO_2; (c) CaO and MnO; and (d) S plotted vs Al_2O_3 for analysis MEG1B.

imbricated. Minimum shortening perpendicular to cleavage calculated from vein imbrication is 30%.

Cleavage zones are defined by concentrations of phyllosilicates. Quartz grains are most commonly elliptical in shape, with long axes paralleling cleavage. Chlorite is present as porphyroblasts in slate layers. Small framboidal pyrite grains are common in slate laminae and have poorly developed pressure shadows. Fiber orientations parallel cleavage in most pressure shadows, although a few show two stages of development, with earlier fibers oriented nearly parallel to bedding.

Bedding and imbricated vein segments are offset along wide (up to 2.5 mm), spaced zones of coalesced cleavage which run at high angles to bedding and parallel to the penetrative cleavage in adjacent rocks. Offset along any individual cleavage zone is consistent for all layers, regardless of cleavage–bedding angle, suggesting a component of cleavage parallel shear. These intense cleavage zones are virtually devoid of quartz and become more diffuse with distance from the calcite vein.

Macroprobe data from DG2-2 were collected in a series of five adjacent map analyses totalling 2838 individual spectra. SiO_2/Al_2O_3 ratios for the five maps were contoured together into one map (Fig. 14). Analyses of vein material, indicated by high CaO values, were eliminated to minimize interference with slate chemistry contouring. SiO_2/Al_2O_3 highs form roughly triangular zones between areas of spaced cleavage. SiO_2 values greater than 70 wt% are common in the triangular zones, with a maximum of 78 wt%. Where SiO_2 is highest, Al_2O_3 ranges between 8 and 10 wt%. Spaced cleavage zones are depleted in SiO_2 with respect to Al_2O_3, with silica values in the centers of these zones between 39 and 45 wt% and Al_2O_3 values up to 30 wt%. Although not shown on the contour map, Fe_2O_3, K_2O, S, TiO_2 and MgO are also enriched in the cleavage zones.

SiO_2 and CaO are plotted vs Al_2O_3 for all 2825 analyses of DG2-2 in Figs. 15(a) & (b). These plots clearly show two compositional domains related to slate and limestone–vein compositions. Analyses with $Al_2O_3 > 9$ wt% and $CaO < 10$ wt% were selected as represen-

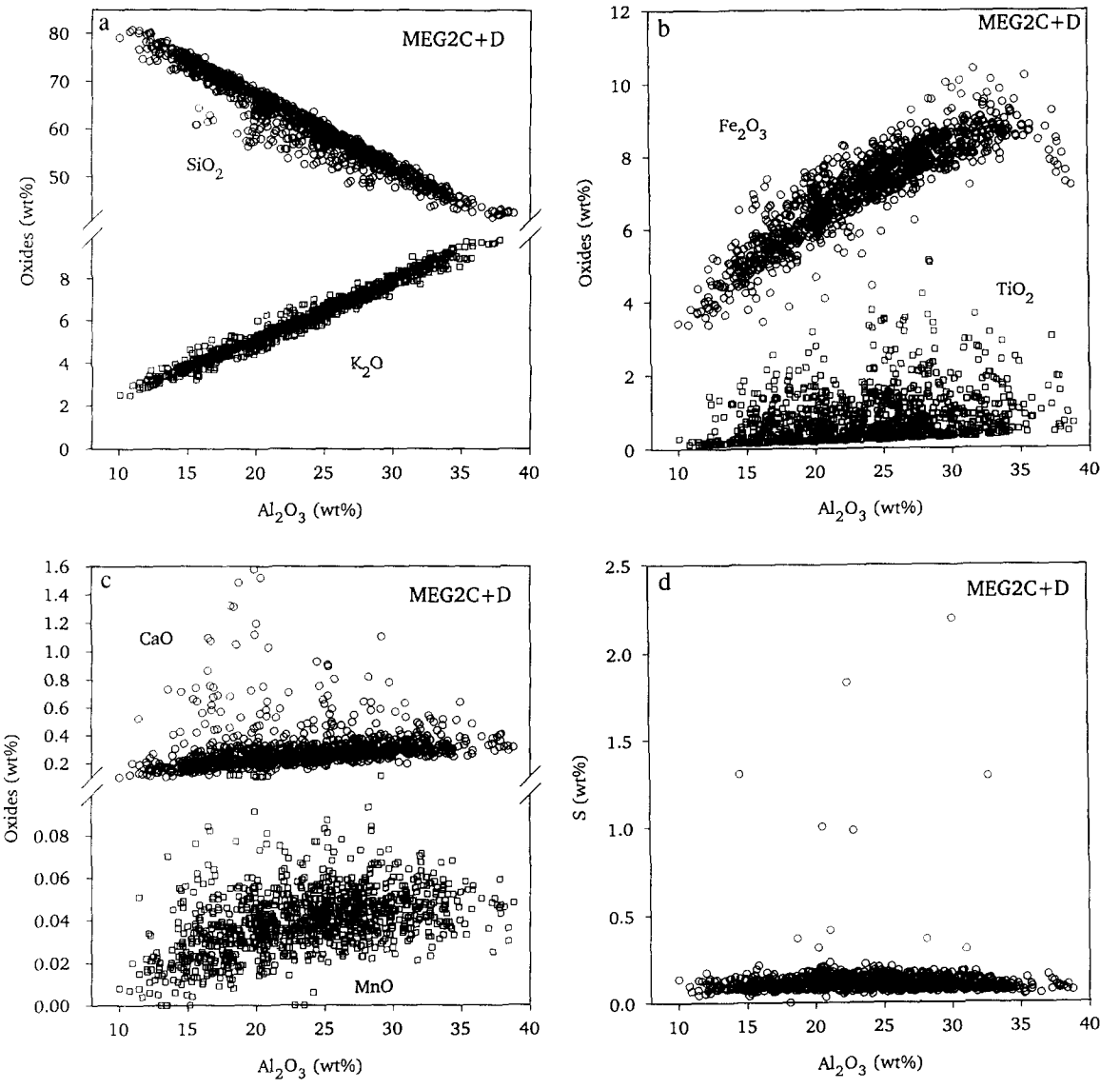

Fig. 8. Variation diagrams showing: (a) SiO_2 and K_2O; (b) Fe_2O_3 and TiO_2; (c) CaO and MnO; and (d) S plotted vs Al_2O_3 for analysis MEG2C+D.

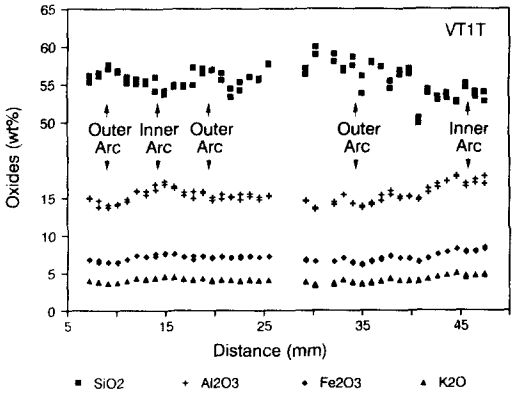

Fig. 9. Profile of composition vs distance for analysis VT1T.

tative of compositional changes within the slates and are plotted vs Al_2O_3 in Figs. 15(c)–(f). Fe_2O_3, K_2O and TiO_2 generally show immobile behavior and SiO_2 is clearly mobile relative to Al_2O_3. When examined in detail, Fe_2O_3 appears to be slightly depleted at higher Al_2O_3 whereas TiO_2 and S are disproportionately enriched relative to Al_2O_3 (see Fig. 3c for TiO_2 plotted vs Al_2O_3 at an expanded scale). MgO increases with increasing Al_2O_3 between 9 and 22 wt% Al_2O_3, but is depleted where Al_2O_3 is greater than 22%. MnO and CaO plotted vs Al_2O_3 are highly scattered, but in general indicate a negative correlation with Al_2O_3 above 15 wt% Al_2O_3 and a positive correlation with Al_2O_3 below 15 wt% Al_2O_3. The abundance of carbonate minerals in this sample suggest that MnO and CaO are dominantly in carbonate minerals. The complexity of these element distributions probably results from the mixture of initial lithologies in this sample and the high intensity of the cleavage zones.

DISCUSSION

Element flux

The distributions of individual oxides and S plotted vs Al_2O_3 are summarized in Fig. 16 by plotting the

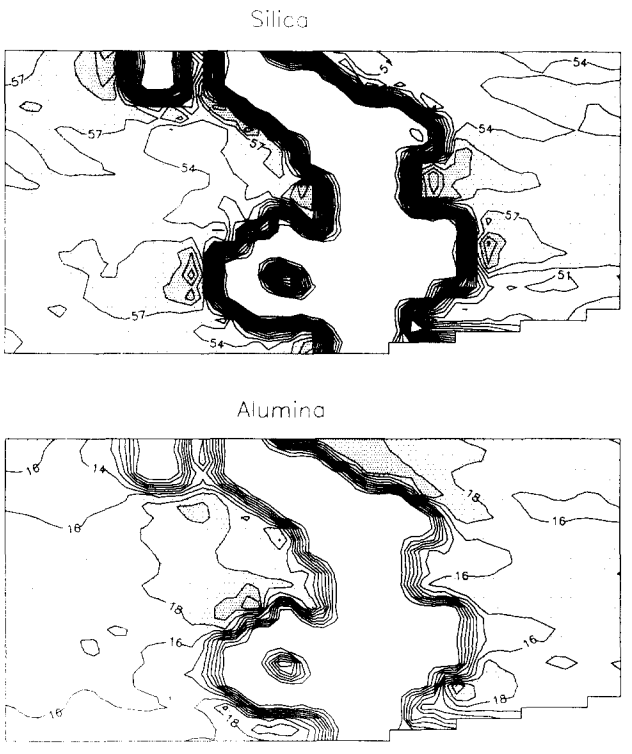

Fig. 10. Contoured (a) SiO_2 and (b) Al_2O_3 maps from analysis VT1M.

regression lines for each data set. The regression coefficients are summarized in Table 2. The bold lines in Fig. 16 show the range of the data and the fine lines show their extrapolation to the y-axis so the intercept can be compared with the idealized behavior shown in Fig. 2.

SiO_2 is well correlated with Al_2O_3 (Fig. 16a), with R^2 ranging from 0.71 to 0.99. In all samples, the consistent negative slopes of the regression lines clearly shows mobile behavior of Si relative to Al. The variability in y-intercepts appears to be largely a function of the differences between the sums of the analyses. If SiO_2 is the only mobile component and the analyses sum to 100%, then the y-intercept should be 100%. The Meguma samples have the highest sums and y-intercepts whereas the Mettawee and Martinsburg have lower sums and y-intercepts.

K_2O shows the best correlation with Al_2O_3, with R^2 ranging from 0.96 to 1.00 (0.997). This excellent correlation is probably due to mineralogic linkage of K with Al in illite and muscovite. The slopes on the lines vary with locality, with the Meguma samples showing lower slopes. With the exception of one set of analyses, the y-intercepts of the regression lines in Fig. 16(b) are negative. The intercepts themselves are clustered by locality, with the lowest intercepts given by the Mettawee slate (−0.96, −1.37), followed by the Martinsburg slates (−0.59 to −0.37) and the Meguma slates (−0.33 to 0.033). The negative intercepts suggest that white micas are more potassic in the aluminous cleavage zones than in the intervening microlithons. This possibility is consistent with the microprobe analyses of Sutton (1989) who found that P domain (cleavage zone) micas were higher in K than adjacent Q domain (microlithon) micas. Sutton (1989) hypothesized that P domain micas were further along the metamorphic transition from illite to muscovite. The different ranges of intercepts for the different localities can be attributed to different degrees of metamorphic recrystallization. The near-zero intercepts for the Meguma slates may be due to a higher metamorphic equilibration indicated by their coarser grain size and greater recrystallization (e.g. development of sphene aggregates).

TiO_2 is also well correlated with Al_2O_3 in the Mettawee analyses and in Martinsburg analyses CM3A and M1A, with R^2 ranging from 0.82 to 0.96. A lower R^2 value of 0.55 and a substantially lower y-intercept for Martinsburg sample DG2-2 is due to the upward bend in the TiO_2 values at high Al_2O_3 contents (Figs. 3c and 16c). This suggests that in the extremely intense cleavage zones of this sample, Al is mobile relative to Ti. The lower R^2 values for the Meguma samples, which range from 0.03 to 0.21, are the result of scatter due to localized Ti segregation in metamorphic sphene porphyroblasts. Despite these low levels of correlation, the positive slopes and near zero y-intercepts suggest immobile behavior of Ti at the hand specimen scale. The analytical scatter simply indicates that Ti is redistributed over a larger volume than the macroprobe sampled for these analyses. In fact, R^2 values appear to increase with increasing spot size: R^2 for analyses with 19 mm^2 spot areas ranged from 0.03 to 0.11 whereas R^2 for analysis MEG1A with a 110 mm^2 spot area was 0.21.

Fe_2O_3 is well correlated with Al_2O_3, with R^2 ranging from 0.58 to 0.90. Once again, the regression lines group with locality, with the lower Fe_2O_3 values for the Meguma samples probably due to differences in original composition. A particularly interesting aspect of these data is that the y-intercepts are all positive, ranging as high as 3.0 wt% Fe_2O_3. Inspection of the individual plots, particularly that of the Meguma samples in Figs. 7(b) and 8(b) shows that Fe_2O_3 concentrations level off or even start to decrease in analyses with the highest Al_2O_3 content. This behavior can be attributed to initial immobile behavior of Fe followed, at higher levels of dissolution, with mobile behavior. Sutton (1989) found that P domain (cleavage zone) micas were depleted in Fe and Mg relative to Q domain micas, which could contribute to a positive y-intercept. She suggested that the chlorite, a probable host for Fe, was preferentially concentrated in Q domains (microlithons) relative to muscovite, consistent with the removal of Fe from the cleavage zones and recrystallization in the microlithons.

CaO and MnO show nearly identical behavior, which varies strongly with rock type. Correlation coefficients are generally low, with R^2 ranging from 0.01 to 0.59. In the Meguma samples, low CaO and MnO values show a positive correlation with Al_2O_3, suggesting that these elements are contained in immobile silicates and sphene. The higher CaO and MnO values in the Martinsburg and Mettawee samples are negatively correlated with Al_2O_3 at high Al_2O_3 contents, suggesting mobility due to dissolution of carbonate. The arch-like distribution of CaO and MnO data points in sample

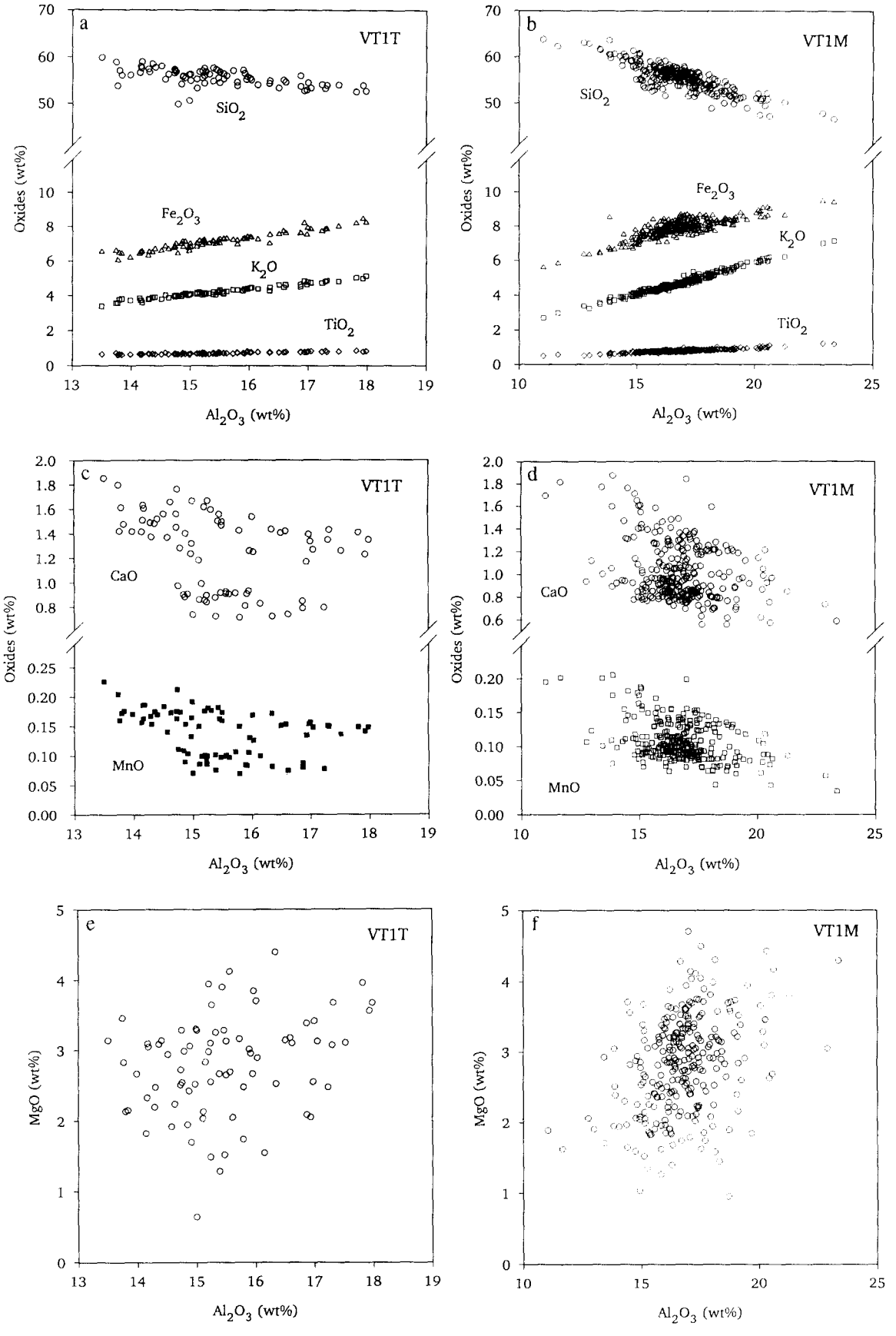

Fig. 11. Variation diagrams showing: (a & b) SiO_2, Fe_2O_3, K_2O and TiO_2; (c & d) CaO and MnO; and (e & f) MgO plotted vs Al_2O_3 for samples VT1T and VT1M.

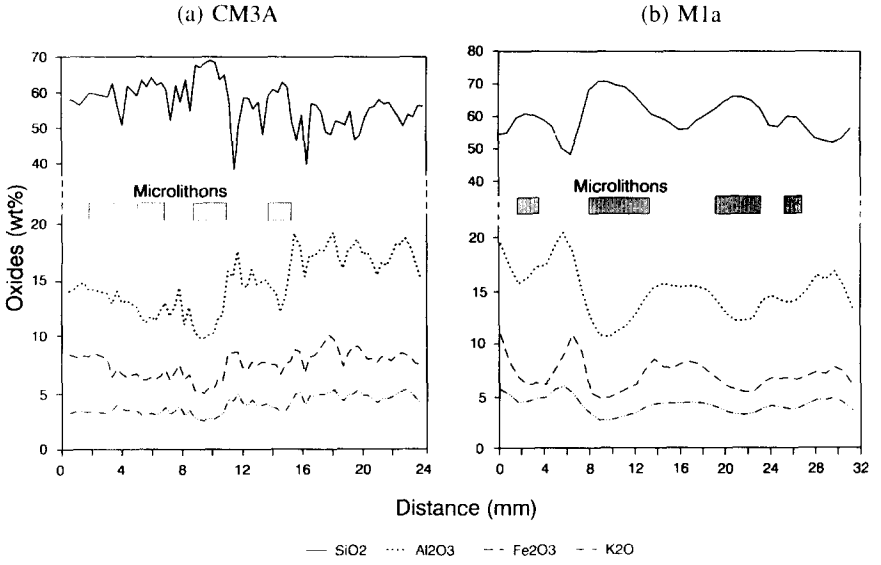

Fig. 12. Profiles of composition vs distance for Martinsburg samples: (a) CM3A; and (b) M1A.

DG2-2 (Fig. 15d) can be explained using Fig. 2 as a reference. The negative slopes of the average curves at high Al_2O_3 values are consistent with depletion by dissolution. The positive slopes at low Al_2O_3 values are consistent with dilution, probably by SiO_2. This suggests that the CaO and MnO mobilized in the aluminous cleavage zones may move outside the slates sampled by these analyses. This hypothesis is supported by the existence of clear carbonate rims on the carbonate beds in adjacent samples (Ward 1991).

In the Meguma samples, Mg was beyond our analytical resolution due to its low abundance and the blocking of low-energy X-rays by the beryllium detector window. In the Martinsburg and Mettawee samples, MgO has a poor positive correlation with Al_2O_3 (R^2 = 0.08–0.38). This variable mobility could be due to immobile MgO in phyllosilicates and mobile MgO in carbonates.

S was also variable in behavior depending on the degree of remobilization of the sulfides. The Mettawee samples contained a few large grains of pyrite indicating a minimum of cm-scale redistribution of Fe and S. S was more evenly distributed in the Martinsburg and Meguma samples where it showed immobile behavior relative to Al with the exception of numerous high S values representing porphyroblasts.

In summary, the only element showing consistent mobility relative to Al_2O_3 is SiO_2, which is low in cleavage zones and high in microlithons. Carbonate-rich slates show CaO and MgO dissolution in cleavage zones. TiO_2 is immobile except for local redistribution in sphene within the higher-grade Meguma slates. K_2O is mineralogically linked to Al_2O_3, with some deviation possibly due to higher K/Al ratios in cleavage zone micas. Iron shows immobile behavior except in very intense cleavage zones where it is depleted. Al_2O_3 appears to be immobile in all but the most intense cleavage zones (DG2-2) where it is depleted relative to TiO_2.

Volume flux

One of the main applications of the macroprobe analyses is in the calculation of volume loss for individual cleavage zones and the rock as a whole. In order to calculate the volume flux from the geochemistry of a sample, existing compositions need to be compared with an initial composition and both compositions converted to volume percent. Previous conversions of weight % analyses to volume % involved the determination of the relative density of the individual analysis areas (Gresen 1967, Gratier 1983). The determination of density on the scale of macroprobe analyses is clearly problematical. But volume changes can also be estimated using an oxygen normalization of the wt% data (Erslev & Mann 1984, Rowan *et al.* 1991). Barth (1952) and Thompson (1982) showed that an oxygen normalization closely approximates a volume normalization because the volume of a mineral is largely determined by its anion content. A plot of molar volume vs moles oxygen per formula unit for common minerals in slates (Fig. 17) shows this excellent correlation (R^2 = 0.98). Because sulfur is close to oxygen in size, the volume of the sulfide, here assumed to be pyrite, can also be approximated.

Normalizing by oxygen content is accomplished by dividing an oxide wt% analysis by the molar weight, multiplying by the number of oxygens (or sulfurs) per formula unit, and then normalizing to 100%. Associated H_2O in muscovite is compensated by adding extra oxygens to each K cation and unanalyzed CO_2 in carbonate is partially compensated by adding two additional oxygens for each CaO. Errors due to uncertainty about the Fe oxidation state, unanalyzed Na in feldspar (for macroprobe analyses) and the existence of additional H_2O in chlorite and other minerals will not seriously effect this calculation.

The choice of an initial composition upon which to

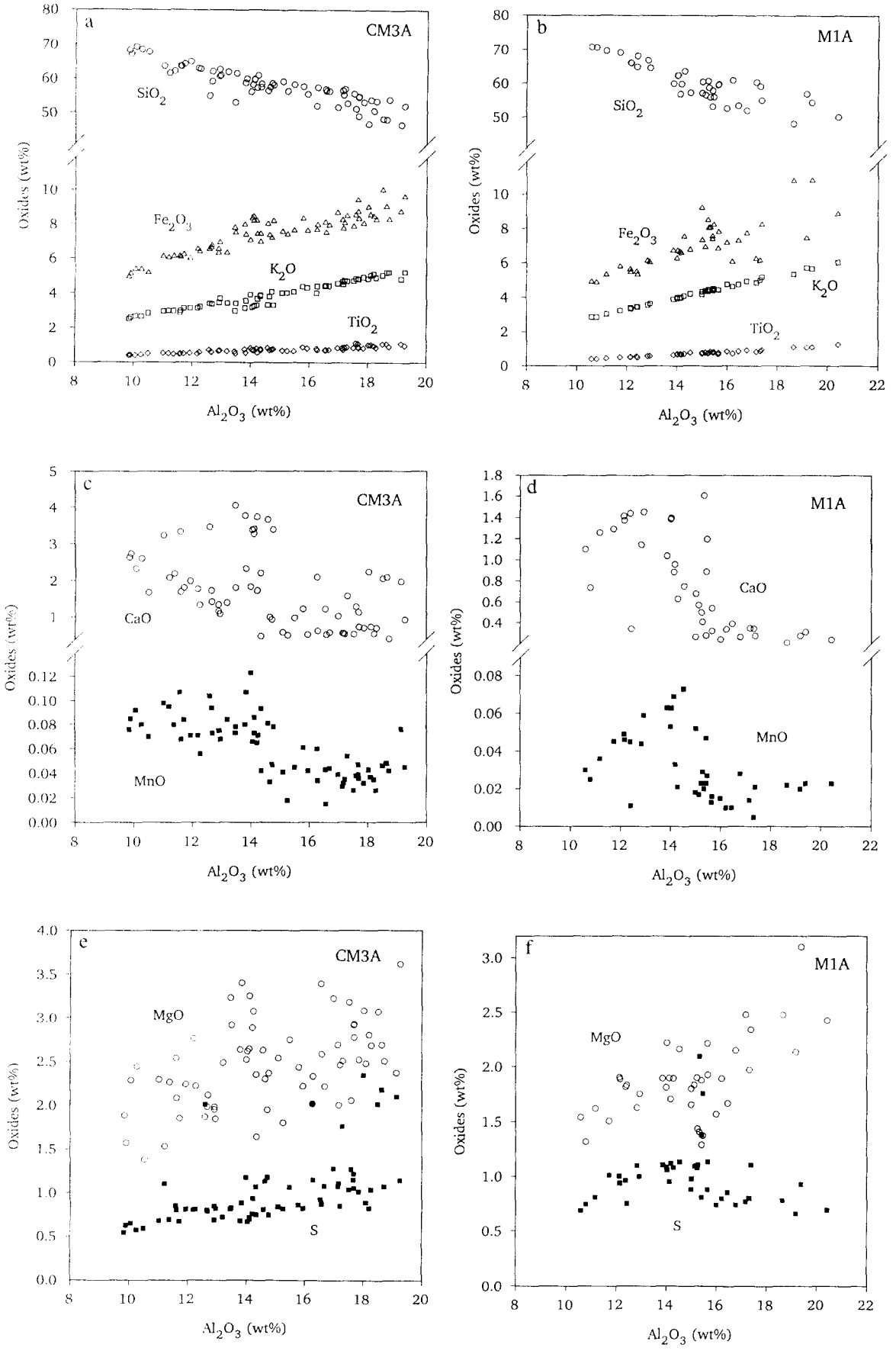

Fig. 13. Variation diagrams showing: (a & b) SiO_2, Fe_2O_3, K_2O and TiO_2; (c & d) CaO and MnO; and (e & f) MgO and S plotted vs Al_2O_3 for samples CM3A and M1A.

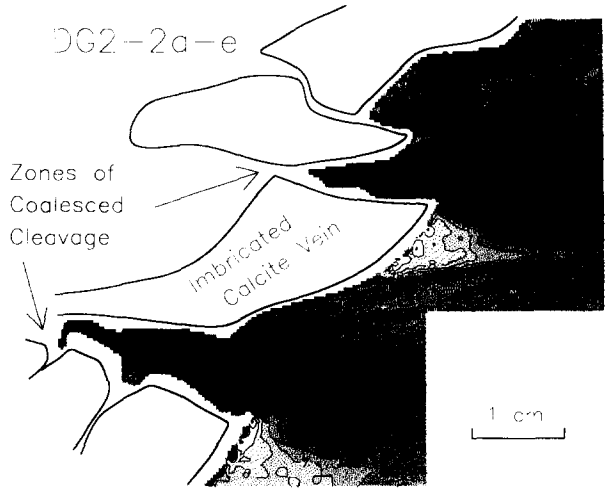

Fig. 14. Contoured SiO_2/Al_2O_3 ratio map from analyses DG2-2a–e.

base volume change calculations is problematical. Erslev & Mann (1984) and Gilfrich *et al.* (1990) assumed that the most siliceous microlithon in sample CM3A represented the initial slate composition. Fortuitously, volume-loss calculated on this basis (42%) is comparable with the shortening parallel to bedding (37–43%) indicated by the imbricated and folded carbonate layers at this locality. But closer examination of the composition of the microlithon used to represent the original composition shows that it is much more siliceous (up to 69 wt% SiO_2 unnormalized) than the average shales in Table 1, which range to 60 wt% SiO_2. This suggests that SiO_2 may have been added to the microlithon, making it a poor choice for an initial composition.

In fact, the average macroprobe analyses in Table 2 are remarkably similar to the average pelite analyses in Table 1, particularly if one compares the normalized analyses with non-volatile components summed to 100%. This can be seen graphically in Fig. 18 which superimposes the average macroprobe and pelite analyses on the area defined by SiO_2–Al_2O_3 regression lines in Fig. 16(a). Both sets of average analyses plot in the center of the field of regression lines, suggesting that dissolution of SiO_2 in the cleavage zones (high Al_2O_3 analyses) is at least partially balanced by enrichment of SiO_2 in the microlithons (low Al_2O_3 analyses).

The hypothesis of local enrichment of SiO_2 in the microlithons is supported by anomalous, triangular-shaped highs in SiO_2 and SiO_2/Al_2O_3 seen immediately adjacent to the outer arcs of folds in the Meguma and Mettawee analyses (Figs. 6 and 10) and between offsets in the calcite vein in DG2-2 (Fig. 14). The local redistribution of Si from cleavage zones to microlithons is shown by plotting two cleavage-parallel traverses from map analysis MEG1b, with one traverse within the outer arc of a fold and the other within the inner arc of a fold (Fig. 19). In the outer arc traverse, SiO_2 steadily decreases from a high of 75 wt% immediately adjacent to the vein to 60 wt% in the penetrative cleavage away from the vein. In the inner arc traverse, SiO_2 increases from 45 wt% in the intense cleavage immediately adjacent to the vein to 58 wt% in the penetratively cleaved slate. Al_2O_3 shows the opposite behavior, increasing away from the outer arc and decreasing away from the inner arc. At 25 mm from the vein, outer arc and inner arc traverse compositions are converging on a composition similar to that of the average pelites in Table 1.

Although the appropriate choice of initial compositions for the samples analyzed in this study is not clear, the similarities between average macroprobe, slate and shale compositions indicate that volume-modeling of an average pelite composition can address the question of large (e.g. 50–60%) volume losses. The North American shale composite (NASC: Gromet *et al.* 1984) was selected as a starting composition due to its intermediate composition relative to other pelite average compositions and its status as the most used average pelite composition. Weight % and volume % (by oxygen normalization) values for the NASC (Fig. 20) show significant increases from weight to volume percent for Si- and Ca-bearing components because Si is associated with two oxygens and Ca with three oxygens (assuming that the Ca is contained in carbonate minerals). In total, SiO_2 and Al_2O_3 account for over 80% of the rock volume.

Because SiO_2 and $CaCO_3$ are the major mobile components in the slates analyzed in this study, volume changes can be approximated as resulting from SiO_2 and $CaCO_3$ flux of NASC (Fig. 21). Because CaO accounts for less than 6 vol% of NASC, complete calcite dissolution would result in minimal (6 vol%) volume loss. SiO_2 is both more consistently mobile and much more abundant, making up 67 vol% of NASC. For 50% volume loss by SiO_2 dissolution, the NASC model in Fig. 21(b) predicts that the average slate would have less than 35 wt% SiO_2 and greater than 30 wt% Al_2O_3. Similar compositions are seen in the most highly cleaved portions of the Meguma and Martinsburg samples, indicating that localized depletion of this magnitude does occur. These compositions, however, are not close to the average compositions of our analyses because they are counter-balanced by high SiO_2 analyses in the adjoining microlithons. To our knowledge, no whole-rock slate analysis approaches the composition predicted by 50% volume loss of NASC.

Another possibility is that the slate compositions represent final compositions after 50% volume loss of a more siliceous protolith than NASC. If we first assume that Si is the only mobile, non-volatile element of significance, the above approach can be inverted to predict the composition of the protolith. Starting with the average composition of the Meguma map analyses (MEG1B and MEG2C+D, Table 2), hypothetical initial compositions were calculated by applying a volume gain of 100% to the average slate compositions. This volume gain applied to the end-product slate is equivalent to a 50% volume loss of the shale protolith. Starting with an average composition of 62.7 wt% SiO_2 and 22.9 wt% Al_2O_3, an original composition of 80.4 wt% SiO_2 and 11.8 wt% Al_2O_3 is required for 50% volume loss. This composition is well beyond the range of the average slate and shale compositions in Table 1.

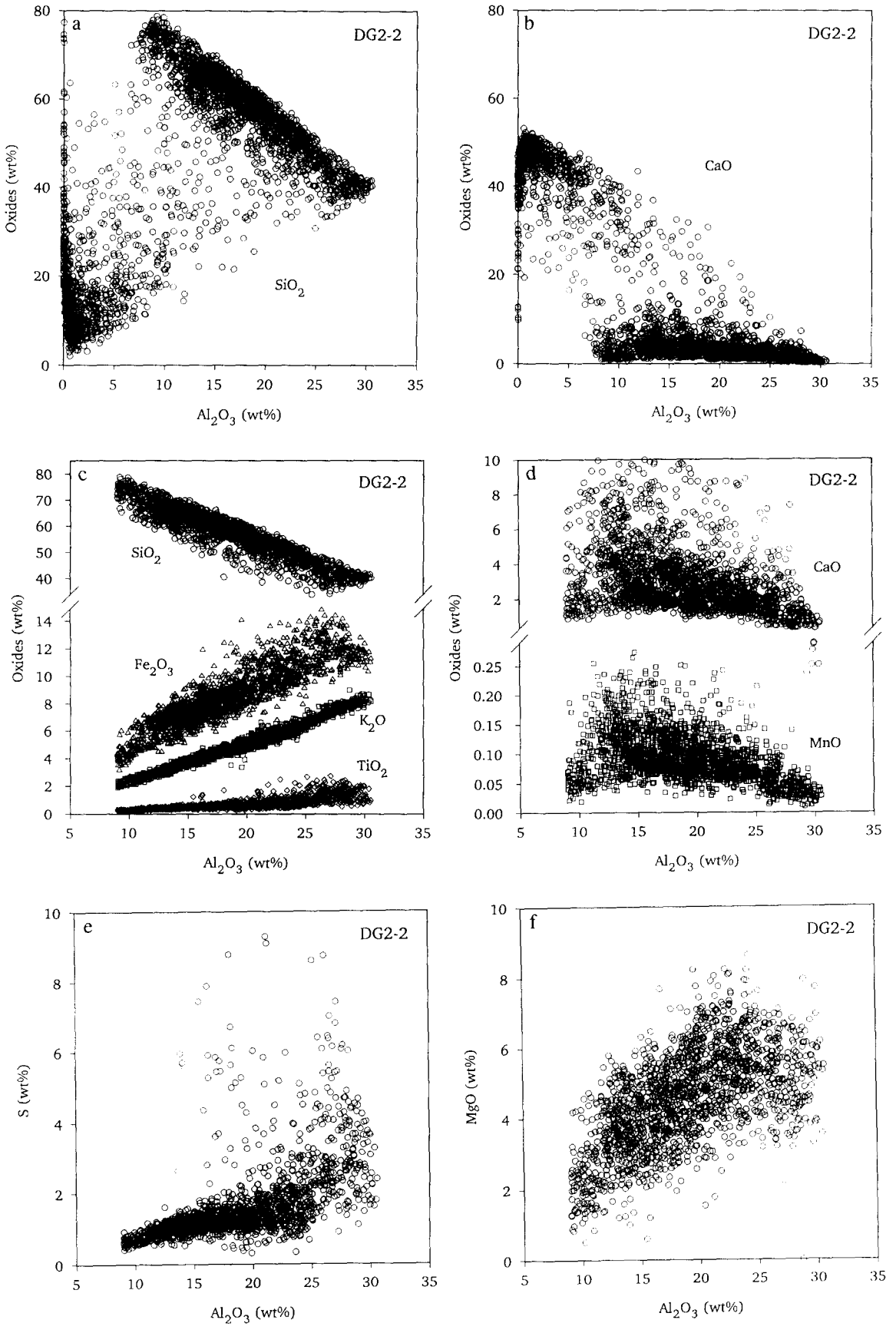

Fig. 15. Variation diagrams showing: (a) SiO_2 and; (b) CaO vs Al_2O_3 for all analyses of the DG2-2 element map; (c) SiO_2, Fe_2O_3, K_2O and TiO_2; (d) CaO and MnO; (e) S; and (f) MgO plotted vs Al_2O_3 for the pelitic subset of these analyses.

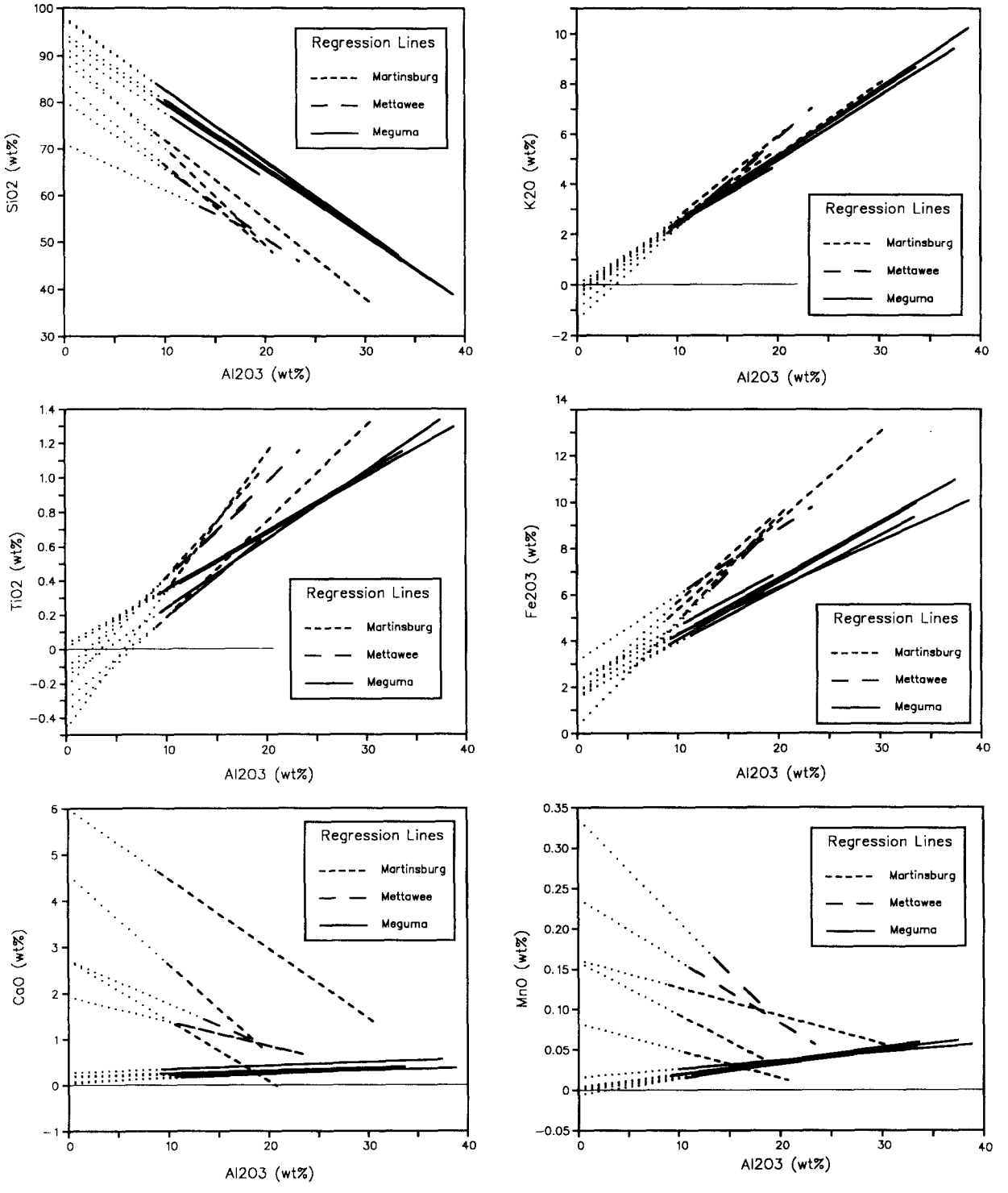

Fig. 16. Linear regressions of oxide analyses plotted vs Al_2O_3 (see Table 2 for summary statistics). Solid and dashed lines show the regression lines within the observed compositional range and dotted lines show their extrapolation to the y-intercept.

To our knowledge, the only slate analyses within 10 wt% SiO_2 of these compositions are the macroprobe analyses of silica-enriched microlithons adjacent to coalesced cleavage zones reported in this paper.

The only shales with SiO_2 contents this high are siliceous shales, which have up to 90 wt% SiO_2 (normalized from Pettijohn 1975). These unusual rocks owe their high silica values to additional components of volcanic ash or biogenic silica. Their environments of deposition do not match those of the slates studied in this paper. Even if the protoliths were less pelitic and more arenaceous, it is difficult to find a conceivable protolith with SiO_2 in the range of 80 wt%. The average graywacke compositions reported by Pettijohn (1975) and Taylor & McLennan (1985) have SiO_2 (normalized) compositions of less than 70 wt%. Thus, compositions of conceivable sedimentary protoliths do not match the compositions required by 50% volume loss of SiO_2 in the

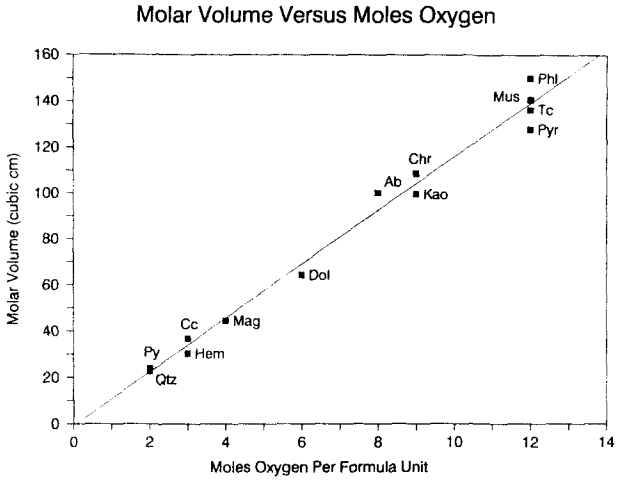

Fig. 17. Correlation of molar volumes (Robie *et al.* 1978) plotted with moles oxygen per formula unit for major minerals occurring in slates ($R^2 = 0.98$).

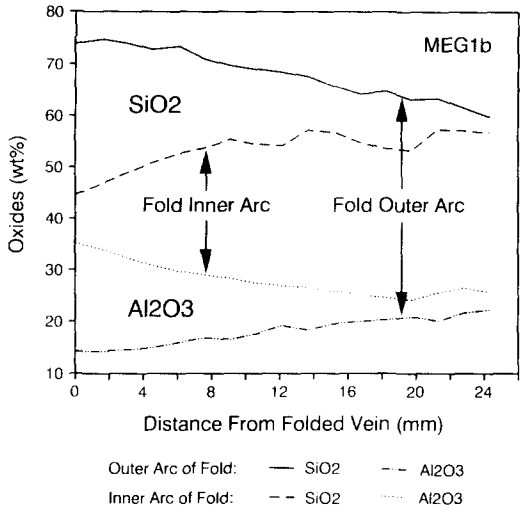

Fig. 19. SiO_2 and Al_2O_3 vs distance from the buckled vein in two cleavage-parallel traverses in analysis MEG1B. One traverse parallels cleavage adjacent to the outer arc of a fold and one parallels cleavage adjacent to the inner arc of the fold.

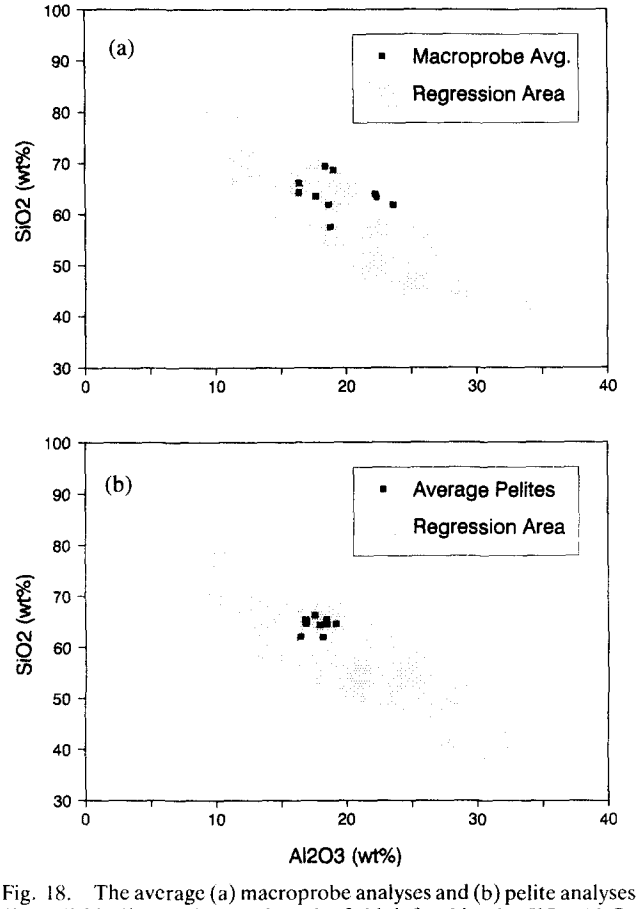

Fig. 18. The average (a) macroprobe analyses and (b) pelite analyses (from Table 1) superimposed on the field defined by the SiO_2–Al_2O_3 regression lines of macroprobe analyses. If the average pelite analyses are representative of the original compositions of the macroprobe analyses, then both volume loss and gain is indicated.

slates analyzed herein. Lesser amounts of SiO_2 depletion (e.g. < 25% volume flux) are possible because of the range of potential initial compositions.

The Martinsburg and Mettawee slates also show Ca mobility, suggesting that the dissolution of a carbonate component in slates could account for a substantial volume reduction. For a slate with a NASC composition, the protolith affected by 50% volume loss by calcite dissolution would have nearly equal SiO_2 and CaO contents (respectively 40.4 and 39.5 wt%, normalized to zero volatile content). But this would require making the slate protoliths into argillaceous limestones, not shales. The local redeposition of carbonate in clear rinds on adjacent carbonate layers in the Martinsburg samples suggests only limited mobility of carbonate.

The remaining mode of accomplishing major (e.g. 50%) non-volatile volume loss in slates would require the wholesale removal of material in nearly the exact proportion of the original composition. In other words, removing material of pelitic composition would leave the residue with the composition of the original pelite. But this is not consistent with the large differences in cleavage zone and microlithon compositions documented by this study. In all of the macroprobe analyses, Si is clearly much more mobile than Al, Ti, Fe or K. Dramatic volume losses would require large changes in major element ratios because the large range of mineral solubilities within slates would result in non-proportional element depletions. This mode of volume loss would also require hydrothermal solutions quite different from those previously documented (White 1957). Eventually, these solutions might be expected to deposit material approximating slate compositions, not the quartz–calcite vein assemblages characteristic of low-grade metamorphism.

In conclusion, slates with heterogeneous cleavage due to argillaceous layers or veins show dramatic changes in composition related to cleavage development. Areas of intense, coalesced cleavage are low in Si and high in Al, K, Ti, Fe and Mg. Adjoining areas of poorly developed cleavage are high in Si and correspondingly low in Al, K, Ti, Fe and Mg. Comparison with the compositions of nearby penetratively cleaved areas and pelite compositions in general indicate that Si is depleted in cleavage zones and enriched in adjacent microlithons. Al, K, Ti, Fe and Mg are concentrated by residual accumulation in

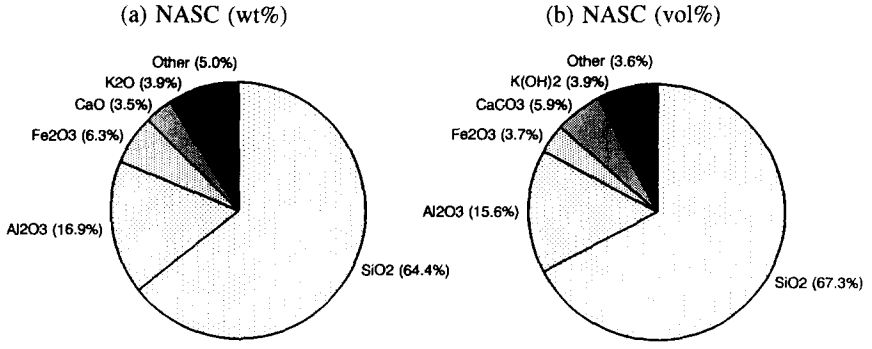

Fig. 20. Comparison of the (a) weight percent composition with the (b) volume percent composition (from oxygen normalization) for the North American shale composite (NASC, Gromet *et al.* 1984).

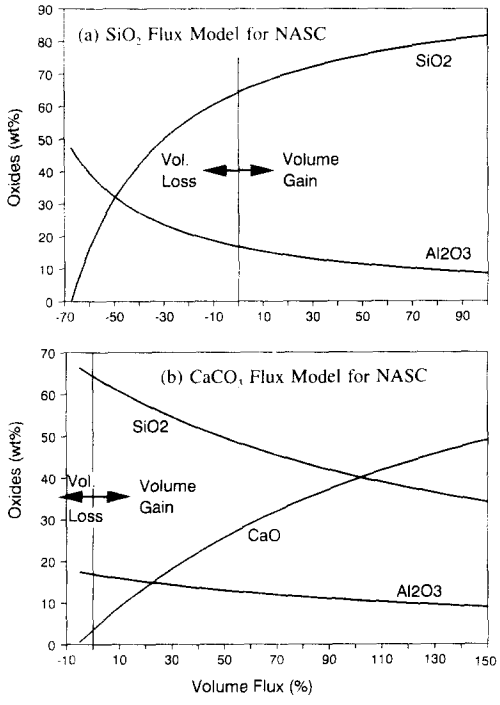

Fig. 21. Predicted changes in SiO_2 and Al_2O_3 wt% compositions due to (a) $CaCO_3$ and (b) SiO_2 flux in a slate with an initial composition equivalent to the North American shale composite (Gromet *et al.* 1984).

cleavage zones and diluted by Si addition to microlithons. Ca and Mn show mobile behavior only when they occur in carbonate minerals.

Comparisons with average pelite compositions indicate that volume flux caused by non-volatile element redistribution is largely limited to the hand-specimen scale, with volume losses in cleavage zones balanced by volume gains in the microlithons. Thus, based on the geochemistry of slates studied in this research, we conclude that shales do not undergo large non-volatile volume losses during the formation of slaty cleavage. The unresolved contradictions between geochemical and geometric calculations of non-volatile volume loss demonstrate the need for integrated geochemical and textural studies of localities suspected of large non-volatile volume losses.

Acknowledgements—This paper has been improved by helpful comments from Art Goldstein, Jack Henderson, Mark McNaught, Sally Sutton and two anonymous reviewers. N. L. Gilfrich Tucker and D. E. Leyden of the Chemistry Department at Colorado State University built the XRF-macroprobe and provided critical XRF expertise. Jack Henderson of the Geological Survey of Canada supplied Meguma slate samples for analysis and Jack Epstein of the United States Geological Survey provided invaluable assistance in collecting samples of Martinsburg slate. Art Goldstein introduced us to the geology of the Vermont slate belt and helped in the sampling. Joseph Taggart of the USGS provided XRF and LECO sulfur analyses of the standards. Peter Shive of the University of Wyoming furnished coring equipment. David T. Lawrence and Shell Offshore Inc. are thanked for their support of this work. The research was supported by grants from the National Science Foundation (EAR-8720824 and EAR-9018426), Texaco and Chevron U.S.A.

REFERENCES

Ague, J. J. 1991. Evidence for major mass transfer and volume strain during regional metamorphism of pelites. *Geology* **19**, 855–858.

Barth, T. F. W. 1952. *Theoretical Petrology*. Wiley, New York.

Bastin, E. S. 1909. Chemical composition as a criterion in identifying metamorphosed sediments. *J. Geol.* **17**, 445–472.

Bell, A. M. 1985. Strain paths during slaty cleavage formation—the role of volume loss. *J. Struct. Geol.* **7**, 563–568.

Beutner, E. C. 1978. Slaty cleavage and related strain in Martinsburg slate, Delaware Water Gap, New Jersey. *Am. J. Sci.* **278**, 1–23.

Beutner, E. C. & Charles, E. G. 1985. Large volume loss during cleavage formation, Hamburg sequence, Pennsylvania. *Geology* **13**, 803–805.

Beutner, E. C. & Diegel, F. A. 1985. Determination of fold kinematics from syntectonic fibers in pressure shadows, Martinsburg Slate, New Jersey. *Am. J. Sci.* **285**, 16–50.

Bhagat, S. S. & Marshak, S. 1990. Microlithon alteration associated with development of solution cleavage in argillaceous limestone: textural, trace-elemental and stable isotope observations. *J. Struct. Geol.* **12**, 39–44.

Boehme, D. R. 1987. X-ray microfluorescence of geological materials. *Adv. X-ray Anal.* **30**, 39–44.

Clarke, F. W. 1924. The data of geochemistry. *Bull. U.S. geol. Surv.* **770**, 1–841.

Clifford, P. M., Rice, M. C., Pryer, L. L. & Fueten, F. 1987. Mass transfer in unmetamorphosed carbonates and during low-grade metamorphism of arenites. In: *Deformation of Sediments and Sedimentary Rocks* (edited by Jones, M. E. & Preston, R. M. F.). *Spec. Publs geol. Soc. Lond.* **29**, 197–209.

Condie, K. C. 1981. *Archean Greenstone Belts*. Elsevier, Amsterdam.

Criss, J. W. & Birks, L. S. 1968. Calculation methods for fluorescent X-ray spectrometry—empirical coefficients vs fundamental parameters. *Analyt. Chem.* **40**, 1080.

Dieterich, J. H. 1970. Computer experiments on mechanics of finite amplitude folds. *Can. J. Earth Sci.* **7**, 467–476.

Durney, D. W. & Ramsay, J. G. 1973. Incremental strains measured by syntectonic crystal growths. In: *Gravity and Tectonics* (edited by Dejong, K. A. & Scholten, R.). John Wiley and Sons, Chichester, 67–96.

Eckel, E. C. 1904. On the chemical composition of American shales and slates. *J. Geol.* **12**, 961–966.

Epstein, J. B. & Epstein, A. G. 1969. Geology of the Valley and Ridge province between Delaware Water Gap and Lehigh Gap, Pennsylvania. In: *Geology of Selected Areas in New Jersey and Pennsylvania and Guidebook of Excursions* (edited by Subitsky, S.), 132–205.

Erslev, E. & Mann, C. 1984. Pressure solution shortening in the Martinsburg Slate, New Jersey. *Proc. Pennsylvania Acad. Sci.* **58**, 84–88.
Ghent, E. & Gordon, T. 1990. Fluids in low and medium-grade metamorphism. In: *Short Course on Fluids in Tectonically Active Regimes of the Continental Crust* (edited by Nesbit, B. E.). Mineralogical Association of Canada, 231–260.
Gibbs, A., Montgomery, C., O'Day, P. & Erslev, E. A. 1986. Geochemistry of Archean and Proterozoic sedimentary rocks and the record of continental crust formation. *Geochim. cosmochim. Acta* **50**, 2125–2141.
Gilfrich, N. L., Leyden, D. E. & Erslev, E. A. 1990. XRF Macroprobe analysis of geologic materials. *Adv. X-ray Anal.* **33**, 593–601.
Gratier, J. P. 1983. Estimation of volume changes by comparative chemical analyses in heterogeneously deformed rocks (folds with mass transfer). *J. Struct. Geol.* **5**, 329–340.
Gresen, R. L. 1967. Composition–volume relationships of metasomatism. *Chem. Geol.* **2**, 47–55.
Gromet, L. P., Dymek, R. F., Haskins, L. A. & Korotev, R. L. 1984. The "North American shale composite": Its compilation, major and trace element characteristics. *Geochim. cosmochim. Acta* **48**, 2469–2482.
Groshong, R. H., Jr. 1976. Strain and pressure solution in the Martinsburg Slate, Delaware Water Gap, New Jersey. *Am. J. Sci.* **276**, 1131–1146.
Henderson, J. R., Wright, T. O. & Henderson, M. N. 1988. A history of cleavage and folding: An example from the Goldenville Formation, Nova Scotia. *Bull. geol. Soc. Am.* **97**, 1354–1366.
Lee, J. M., Peacor, D. R., Lewis, D. D. & Wintsch, R. P. 1986. Evidence for syntectonic crystallization for the mudstone to slate transition at Lehigh Gap, Pennsylvania. *J. Struct. Geol.* **8**, 767–780.
Leyden, D. E. 1984. Fundamentals of X-ray spectrometry as applied to energy dispersive techniques. *Tracor X-ray User School Handbook*.
Lincoln, B. Z. 1988. Transmission electron microscope study of bedding–cleavage relations in the Vassalboro Formation, east-central Maine. *Maine geol. Surv. Stud. Maine Geol.* **1**, 1129–135.
Kanagawa, K. 1991. Change in dominant mechanisms for phyllosilicate preferred orientation during cleavage development in the Kitakami slates of NE Japan. *J. Struct. Geol.* **13**, 927–943.
Krauskopf, K. B. 1967. *Introduction to Geochemistry*. McGraw-Hill, New York.
Mehnert, K. R. 1969. Composition and abundance of common metamorphic rock types. In: *Handbook of Geochemistry* 1 (edited by Wedepohl, K. H.). Springer, Berlin, 272–296.
O'Hara, K. & Blackburn, W. H. 1989. Volume loss model for trace-element enrichments in mylonites. *Geology* **17**, 524–727.
Pettijohn, F. J. 1975. *Sedimentary Rocks* (3rd edn). Harper and Row, New York.
Poldervaart, A. 1955. Chemistry of the Earth's crust. *Spec. Pap. geol. Soc. Am.* **62**, 119–144.
Ramsay, J. G. 1967. *Folding and Fracturing of Rocks*. McGraw-Hill, New York.
Ramsay, J. G. & Wood, D. S. 1973. The geometric effects of volume change during deformation processes. *Tectonophysics* **16**, 263–277.
Robie, R. A., Hemingway, B. S. & Fisher, J. R. 1978. Thermodynamic properties of minerals and related substrates at 298.15° and 1 bar (10^5 pascals) pressure and at higher temperatures. *Bull U.S. geol. Surv.* **1452**.
Rowan, M. G., Kligfield, R. & Erslev, E. A. 1991. Volume flux during folding in the Helvetic nappes, Switzerland. *Geology* **19**, 1001–1004.
Sangster, A. L. 1990. Metallogeny of the Meguma Terrane, Nova Scotia. In: *Mineral Deposit Studies in Nova Scotia* (edited by Sangster, A. L.). *Geol. Surv. Can. Pap.* **90-8**, 115–162.
Shaw, D. M. 1956. Geochemistry of pelitic rocks. Part III: Major elements and general geochemistry. *Bull. geol. Soc. Am.* **67**, 919–934.
Sorby, H. C. 1853. On slaty cleavage, as exhibited in the Devonian limestones of Devonshire. *Phil. Mag.* **11**, 20–37.
Stephens, M. B., Glasson, M. J. & Keays, R. R. 1979. Structural and chemical aspects of metamorphic layering development in metasediments from Clunes, Australia. *Am. J. Sci.* **279**, 129–160.
Sutton, S. J. 1989. Orientation-dependent "metamorphic grade" in phyllosilicates belonging to a slaty cleavage fabric. *J. Geol.* **97**, 197–208.
Taylor, S. R. & McLennan, S. M. 1985. *The Continental Crust: Its Composition and Evolution*. Blackwell Scientific, Oxford.
Thompson, J. B., Jr. 1982. Composition space: an algebraic and geometric approach. In: *Characterization of Metamorphism Through Mineral Equilibria* (edited by Ferry, J. M.). *Miner. Soc. Am. Rev. Miner.* **10**, 1–32.
Tucker, N. L. G. 1992. X-ray fluorescence macroprobe analysis of slates and matrix assisted laser desorption of biomolecules. Unpublished Ph.D. thesis, Colorado State University, Fort Collins, Colorado.Ward, D. J. 1991. Cleavage formation and element flux in argillaceous rocks with non-argillaceous interlayering. Unpublished M.S. thesis, Colorado State University, Fort Collins, Colorado.
White, D. E. 1957. Magmatic, connate, and metamorphic waters. *Bull. geol. Soc. Am.* **68**, 1659–1682.
Wintsch, R. P., Kvale, C. M. & Kisch, H. J. 1991. Open-system, constant-volume development of slaty cleavage, and strain induced replacement reactions in the Martinsburg Formation, Lehigh Gap, Pennsylvania. *Bull. geol. Soc. Am.* **103**, 916–927.
Wright, T. O. & Henderson, J. R. 1992. Volume loss during cleavage formation in the Meguma Group, Nova Scotia, Canada. *J. Struct. Geol.* **14**, 281–290.
Wright, T. O. & Platt, L. B. 1982. Pressure dissolution and cleavage in the Martinsburg Shale. *Am. J. Sci.* **282**, 122–135.

APPENDIX

CSU XRF-MACROPROBE ANALYTICAL PROCEDURES

Instrumentation

The XRF-macroprobe consists of an energy-dispersive X-ray detector and a 50 W, Rh-anode X-ray tube mounted on a stainless steel vacuum chamber (Fig. 1). Incident angles between the sample and both the tube and detector snouts are 45°. The X-ray tube produces a micro-focused beam which is collimated with perforated molybdenum disks to generate an elliptical spot on the sample ranging from 0.7 × 1.0 to 20 × 30 mm in size. The chamber contains a computer-controlled translational stage onto which samples up to 16 cm in diameter are mounted for analysis. The sample may be viewed during analysis through a leaded glass window using a binocular microscope mounted on top of the chamber.

The Si (Li) energy dispersive detector is liquid nitrogen cooled, with a detector area of 30 mm^2 and a beryllium window which can detect characteristic X-rays from elements heavier than sodium. Custom software allows automated spectrum acquisition and translational stage positioning over a pre-selected traverse or grid. After spectrum acquisition, the software converts the spectra to weight percent values using fundamental parameters calculations calibrated with spectra collected from standards (Criss & Birks 1968).

A homogeneous black-board slate and a pressed pellet of 99.9% pure reagent $CaCO_3$ powder were used as standards for the analyses. The composition of the slate standard was determined at the USGS in Denver, Colorado, using wavelength dispersive XRF (CSU-1: Table 1). Used in conjunction, the two standards approximate the compositions of end-member limestones and slates.

Sample preparation and analytical conditions

In order to minimize the effects of weathering, samples were collected from road cuts (Martinsburg Formation), an abandoned quarry (Mettawee Formation) or drill core (Meguma Group). The need for fresh samples made it impossible to sample some classical areas for volume loss. For instance, the weathering needed to highlight graptolites makes the localities documented by Wright & Platt (1982) unacceptable for macroprobe samples. Samples were cut perpendicular to both cleavage and bedding (or veins). To prepare samples for macroprobe analysis, one half of each sample was cast cut-side-down in an epoxy puck and polished. Final polish was achieved using 6 micron diamond paste after ultrasonic cleaning of the sample. The remaining cut face of the sample, which mirrored the polished surface of the macroprobe sample, was thin-sectioned to insure a close match between thin-sections and macroprobe samples.

Each analysis consisted of a series of spot analyses linked together as a line traverse or a map. Using the software, the location of each spot is fixed by selecting x–y co-ordinates of start and finish points of the traverse or map and by selecting the number of increments between spots in both x- and y-directions. Increments in the x- and y-directions were varied with spot size to overlap spots by at least 40%. Overlap minimizes sampling errors induced by the possibility that very thin

Table A1. Accuracy and precision of XRF Macroprobe analyses (after Gilfrich *et al.* 1990)

	W91			W92		
	USGS*	Macroprobe		USGS*	Macroprobe	
	wt%	wt% (SD)†	Normalized‡	wt%	wt% (SD)†	Normalized‡
SiO_2	60.5	61.5(0.2)	59.88	53.4	51.0(1.0)	54.78
Al_2O_3	12.1	12.1(0.1)	11.78	14.7	12.9(0.3)	13.86
Fe_2O_3	8.33	8.40(0.01)	8.18	8.76	7.22(0.24)	7.75
MgO	4.80	5.56(0.17)	5.41	3.10	2.84(0.17)	3.05
CaO	2.44	2.84(0.01)	2.77	5.98	5.89(0.32)	6.33
K_2O	4.20	4.43(0.01)	4.31	3.42	3.24(0.10)	3.48
TiO_2	0.53	0.58(0.004)	0.56	0.76	0.77(0.04)	0.83
MnO	0.39	0.40(0.007)	0.39	0.11	0.10(0.004)	0.11
S	ND§	0.13(0.001)	0.13	0.82	0.81(0.17)	0.87
Total	93.29	95.94	93.42	91.05	84.77	91.06

*XRF whole-rock and LECO sulfur analyses by J. Taggart, USGS.
†Average and standard deviation of XRF macroprobe analyses.
‡Macroprobe analyses normalized to USGS totals.
§Not analyzed.

features (e.g. solutional seams) may fall between spots without sufficient overlap and not be analyzed. For each sample, spot size was selected to be smaller than the width of the smallest microlithon between spaced cleavage zones, but much larger than the largest grains, thus insuring that the bulk composition of microlithon material is obtained. In most cases, samples were oriented so the long axis of the X-ray spot (x-direction) paralleled cleavage, thus minimizing the number of cleavage domains sampled by each spot.

The duration of each spot analysis is determined by the 'live time' selected—the time during which the detector is actually receiving X-rays. 'Dead time', the time the detector is counting previously acquired X-rays without accepting more, is set by adjusting tube current. Tube current for each analysis was optimized so that maximum dead time was near but not above 50% (Leyden 1984). For most analyses tube current was set at 1.25 mA. Most traverses were run with 500 s of live time, with 100 s used for most maps in order to keep total running times under 2 days. The use of 100 s live times reduces analytical precision, but not so much that the analysis is qualitative (Gilfrich *et al.* 1990).

Tube voltage for each analysis is set 5 kV higher than the highest k-line energy of the elements to be excited. Because this study concentrated on major elements in slates and carbonates, 12 kV (5 kV higher than the k-line excitation energy for Fe) was used for almost all analyses. Using 12 kV, elements found in concentrations above 1 wt% in the samples, including Si, Al, Fe, Ca, K, Mg, Ti, Mn and S, can be effectively excited. The detailed macroprobe operating conditions for each set of analyses are tabulated in Ward (1991).

Once start and finish points, spot size, live time, dead time, current and voltage are set, the instrument automatically steps through the programmed points, collecting a spectrum at each one. After all the spectra are saved, multiple spectra are collected on standards using the same X-ray conditions. Unknown spectra are converted to background-subtracted peak intensities and processed using the fundamental parameters software by comparison with the peak intensities of the standards.

Precision and accuracy of macroprobe analyses

The 50 W X-ray tube allows effective k-shell excitation of elements from Mg to Nd. Gilfrich *et al.* (1990) evaluated the accuracy and precision of macroprobe analyses by comparing macroprobe analyses of Wards catalog slates 91 and 92 with whole-rock XRF analyses of the same samples determined at the U.S. Geological Survey by J. Taggart (Table A1). The results show lower standard deviations for W91 because W92 is more heterogeneous, with visible quartz, carbonate and pyrite concentrations. MgO standard deviations are consistently high because of poor counting statistics due to the blockage of low-energy X-rays by the beryllium detector window. Overlap between Rh l-line and S k-line energies complicates quantitative analysis of S, but software used in spectrum processing minimizes this problem. Macroprobe analyses of S content in W92 showed only 1% difference relative to USGS compositions from a LECO sulfur analyzer. Iron is reported as Fe_2O_3 since XRF analyses can not determine the oxidation state. Normalizing the macroprobe averages in Table A1 to a constant difference gives values closer to USGS values.

One important source of error is the heterogeneity of the samples. Attempts to standardize on a homogeneous glass derived from melting slate CSU-1 in a platinum crucible were abandoned when several elements gave consistently erroneous values. This can be attributed to the differences in X-ray absorption in glasses relative to fine grained aggregates of minerals (slate). As a result, all analyses were standardized with fine-grained mineralogic aggregates, a homogeneous blackboard slate (CSU-1, Table 1) and a pressed $CaCO_3$ pellet.

Different slates have unique emission and absorption properties. Examination of the average macroprobe analyses tabulated in Table 2 show that difference values (diff. = 100% − sum of analyzed components) vary with locality, with the Mettawee samples giving the highest differences (12.74 and 10.29 wt%) and the Meguma samples giving the lowest differences (0.10–3.89 wt%). Experiments with the effect of sample elevation showed that these differences are too large and consistent to be the result of changes in sample height. They are probably the result of variations in X-ray absorption and emission efficiency for each sample. But since the absorption of X-rays by each component, including the difference (largely Na_2O, CO_2 and H_2O), is used by the fundamental parameters program, changes in the difference can cause variations of up to 5% for some element ratios.

Thus, the analytical accuracy of individual macroprobe analyses is difficult to determine because differences in X-ray emission and absorption between the standards and the unknowns will vary. The errors inherent in these data suggest that the best use for individual analyses is for comparison within data sets. Comparison between data sets is facilitated by the normalized values in Table 2 where the difference is set to zero. We acknowledge that these semi-quantitative analyses sacrifice accuracy for spatial resolution and do not have either the precision or the accuracy of conventional bulk-rock analyses.